WEAT Report No. 16

UNIVERSITY OF OKLAHOMA OFFICE OF RESEARCH ADMINISTRATION

ATMOSPHERIC RESEARCH LABORATORY

Norman, Oklahoma

VARIATICNAL OPTIMIZATION ANALYSIS OF TEMPERATURE AND MOISTURE ADVECTION IN A SEVERE STORM ENVIRONMENT

by

Marshall J. McFarland

This research was supported

by

National Aeronautics and Space Administration

Contract NAS 9-13360

May, 1975

UNIVERSITY OF OKLAHOMA OFFICE OF RESEARCH ADMINISTRATION

ATMOSPHERIC RESEARCH LABORATORY

Norman, Oklahoma

VARIATIONAL OPTIMIZATION ANALYSIS OF TEMPERATURE AND MOISTURE ADVECTION IN A SEVERE STORM ENVIRONMENT

by

Marshall J. McFarland

This research was supported

by

National Aeronautics and Space Administration

Contract NAS 9-13360

May, 1975

ABSTRACT

Horizontal wind components, potential temperature, and mixing ratio fields associated with a severe storm environment in the south central U.S. were objectively analyzed from synoptic upper air observations with a non-homogeneous, anisotropic weighting function. The grid dimensions of the area of study were near 125 kilometers horizontally and 50 millibars vertically at 18 pressure levels. Each data field was filtered with variational optimization analysis techniques. The vertical motion field was then analyzed using variational optimization analysis to insure that the three-component wind field satisfied mass continuity. The local time change of potential temperature and mixing ratio was determined in order to correlate the temperature and moisture advection patterns with severe storm development. A variational optimization analysis model containing the four dimensional advection equation was used to produce advective forecasts of the potential temperature and mixing ratio fields.

For the data base of 26/1200Z May 1973, several major findings emerged. The dry intrusion is characterized by warm air, the advection of which produces a well defined upward motion pattern. A corresponding downward motion pattern apparently comprising a deep vertical circulation in the warm air sector of the associated low pressure system was detected. Another major result was the alignment of the axes of maximum dry and warm advection with the axis of the tornado producing squall line that subsequently developed.

ACKNOWLEDGMENTS

This research was conducted under SKYLAB Experiment Project Number 582, Severe Storm Environments by Drs. D. E. Pitts, Y. Sasaki, and Mr. J. T. Lee and under National Aeronautics and Space Administration contract NAS 9-13360 with Professor Y. Sasaki of the University of Oklahoma.

This report is the expansion by the addition of Appendix C of the dissertation prepared during my doctoral program supervised by Dr. C. E. Duchon and assisted by Dr. Y. K. Sasaki, Dr. E. M. Wilkins, Dr. J. F. Harp, and Dr. D. G. Decoursey.

TABLE OF CONTENTS

LIST OF TABLES

LIST OF FIGURES

VARIATIONAL OPTIMIZATION ANALYSIS OF TEMPERATURE AND MOISTURE ADVECTION IN A SEVERE STORM ENVIRONMENT

CHAPTER I

INTRODUCTION

The environment of the severe thunderstorm has been subjected to intense study in recent years in an effort to understand the processes occurring within the severe thunderstorm that produce high surface winds, large hail, flood-producing heavy rains, and tornadoes. As the knowledge of these processes increases, so does the ability of meteorologists to accurately predict and perhaps eventually modify the occurrence and severity of these damaging phenomena.

Empirical research, most notably by Miller (1972), provides very important relationships between synoptic and meso-scale features and the processes occurring on the individual thunderstorm scale. The basic reason for this is that the larger scale phenomena are continuous spatially and temporally and are subject to adequate measurement by a variety of techniques; processes occurring on the scale of the thunderstorm are very difficult to measure. Since the thunderstorm's primary source of energy appears to be the buoyancy generated by latent heat release in a conditionally unstable atmosphere, studies of the moisture transport in a severe storm environment have been very encouraging (McGinley, 1973; Sasaki, 1973; Lewis, 1971; Sasaki and Lewis, 1970; and Hylton, 1972). These studies emphasize the high correlation between moisture convergence in the lower atmosphere and the occurrence and development of severe storms.

The determination of moisture, expressed as precipitable water (water mass per unit area) and the time change of moisture, which can be correlated with precipitation (Palmen, 1967) have also been used with success in the analysis of thunderstorm occurrence and precipitation amounts with the storms.

Temperature advection studies should prove equally valuable. In addition to identifying the environmental stability changes produced by differential temperature advection, important clues to the dynamics of squall line development should result. Miller (1972) stresses the presence of a lower level warm air intrusion as a locator for severe storm development. The dynamic reasoning for this appears to be linked to the strong upward motions, produced by warm air advection, that are conducive to severe storm occurrence. Pfeffer (1962) suggests that thermal advection in the lower troposphere dominates over the vorticity advection in determining vertical motion fields for smaller scale phenomena. Morris (1972) also cites the predominance of thermal advection over vorticity advection in producing vertical motions.

The relationship between vertical motion, vorticity advection, and thickness, or thermal, advection is best described by the omega equation developed from the primitive equations of meteorology. The omega equation is a diagnostic expression for the vertical wind component, ω, that is not reliant upon accurate measurements of the horizontal winds. Although the "ω-equation" is based on the geostrophic wind approximation and the lower atmosphere has non-geostrophic components, an examination of the ω-equation will provide insight into the processes which produce vertical motion. In vector form, the ω-equation

simplified (from Holton, 1972) is

$$-\omega \propto C_1 \frac{\partial}{\partial p} [\, \underline{V} \cdot \underline{\nabla} \eta \,] - C_2 [\, \underline{V} \cdot \underline{\nabla} \theta \,]$$

where ω = vertical motion, downward motion is positive

$\underline{V}$ = horizontal vector wind

$\underline{\nabla}$ = horizontal difference operator, a vector

C_1, C_2 = positive constants when evaluated at constant pressure

η = absolute vorticity, the sum of relative vorticity and coriolis acceleration

θ = potential temperature

The first term on the right hand side is the differential vorticity advection term, a term which normally predominates in the atmosphere. The second term is the thickness advection term. Upward vertical motion results from an increase with height of positive vorticity advection, a condition normally found from a trough axis to the downstream ridge axis. This requires that the winds increase with height due to the $(\frac{\partial}{\partial p} \underline{V})$ term; if the winds are invariant with height, then there is no contribution to vertical motion from differential vorticity advection.

The thickness advection term produces upward vertical motion for warm air advection ($\underline{V} \cdot \underline{\nabla} \theta$ is negative for warm air advection). This term is ordinarily small in the atmosphere because the isotherms parallel the wind streamlines (or height contours), but in developing baroclinic systems, the temperature advection term is substantial.

The synoptic situations formed by the severe thunderstorm in the Great Plains all include a developing baroclinic low pressure system

with pronounced thermal advection patterns (Miller, 1972). Many of these systems initially develop as a warm-core dynamic low pressure center as a result of cyclogenesis in the lee trough, a warm core trough formed from a combination of southerly warm flow, subsiding air across the Rocky Mountains and horizontal warm advection from the higher terrain to the west. The latter two mechanisms indicate that the warm air is very dry in the lower layers. This warm air is then advected eastward and northward as the low pressure center continues to develop. This is illustrated in Figures 1 and 2 at the 850 mb level and the 700 mb level for one of the investigative case studies of this paper.

From the author's synoptic experience, the wind profile in the southeast sector of cyclogenesis in the lee trough is largely invariant with height through the lower and middle levels (occasionally to the 500 mb level) coincident with the thermal ridge in the low levels. This suggests that the environmental vertical motion field may be largely determined by the thickness advection, which can be determined by evaluation of temperature advection. One example of the magnitude of the warm air advection is shown in Figure 3. The soundings are for Tinker AFB, Oklahoma on 26/00Z and 26/12Z, May 1973. A tornado producing squall line occurred in eastern Oklahoma later on in the day.

In severe storm environments, the source for much of the heat energy appears to be radiational heating of the higher terrain of eastern New Mexico, the High Plains of Texas and western Oklahoma. In severe storm synoptic situations, the cloud-free dry air to the west of the surface location of a maximum dew-point temperature gradient heats rapidly. Since the lower portions of this air mass have a near dry-

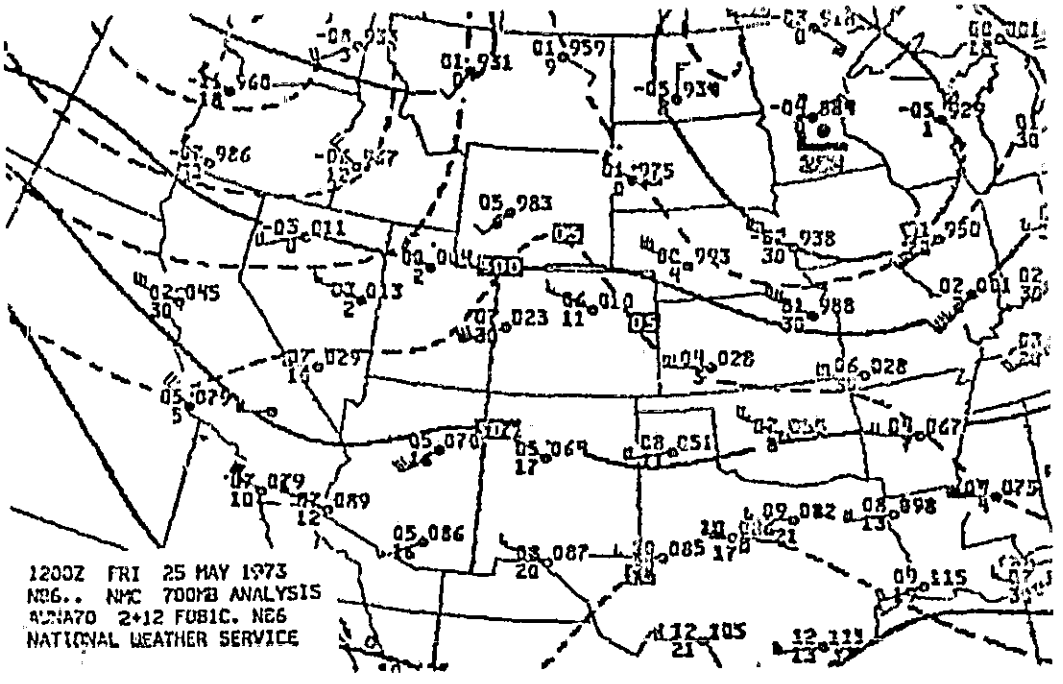

Figure 1a.

Figure 1a-1c. The 700 mb analyses for 25/1200Z, 26/1200Z, and 27/1200Z May 1973. The synoptic patterns illustrate the pronounced warm-core nature of cyclogenesis and frontogenesis in the lee of the mountains trough, which is especially evident in Figure 1b. During the transition from the warm core low to the cold core low in Figure 1c, warm advection is pronounced to the east of the trough axis. This is followed by the pronounced cold advection to the west as the low changes to a cold core structure.

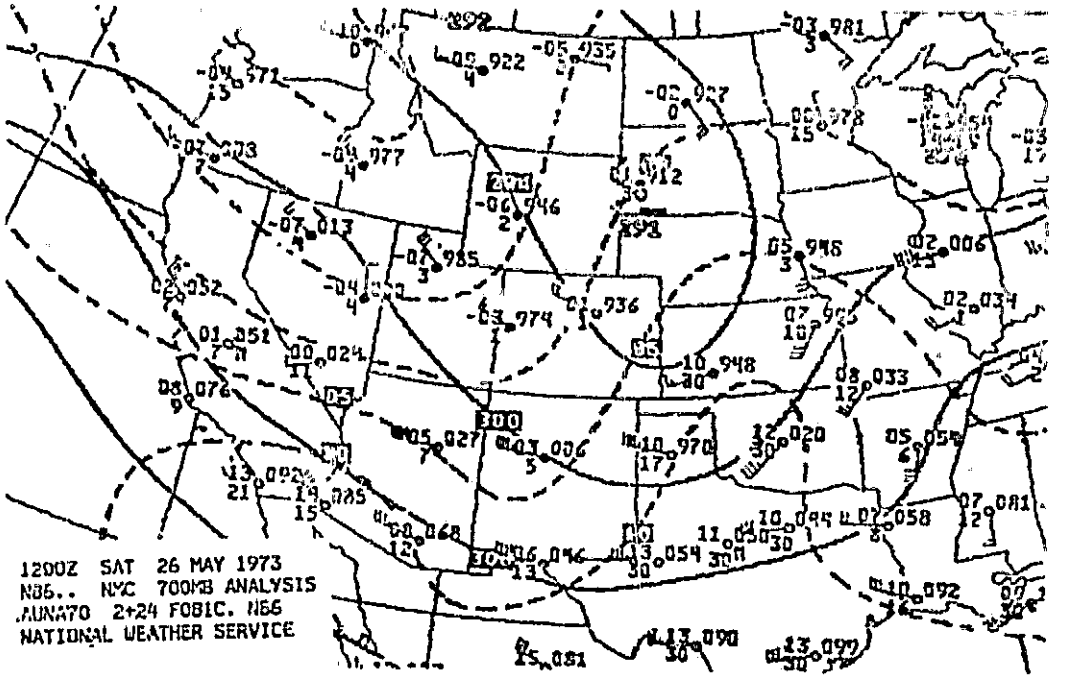

Figure 1b.

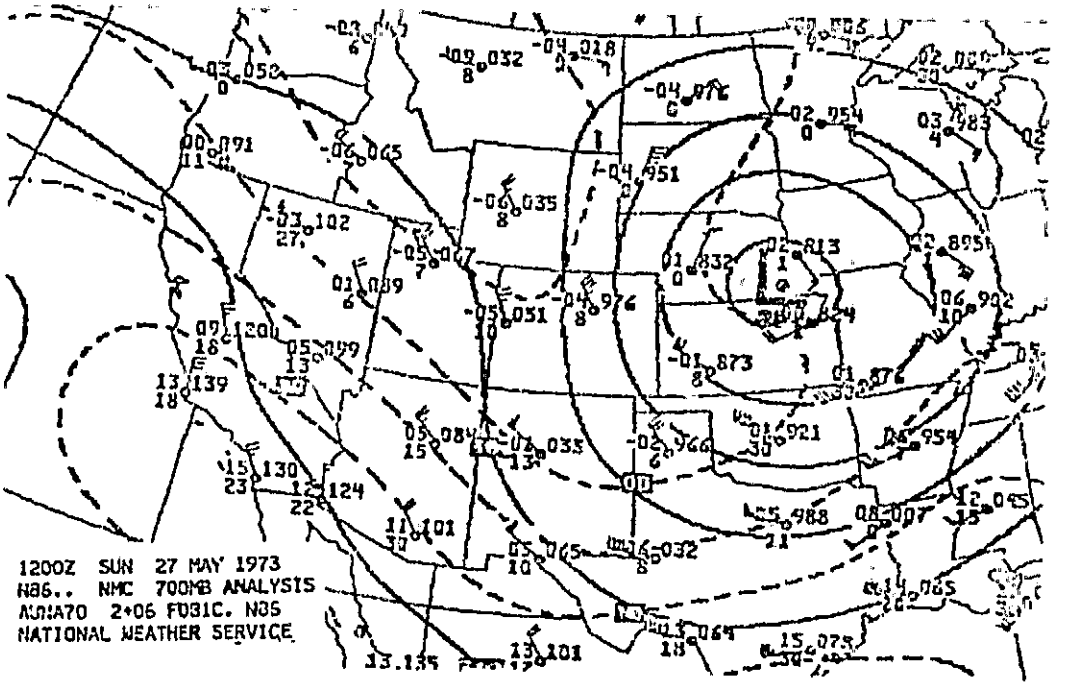

Figure 1c.

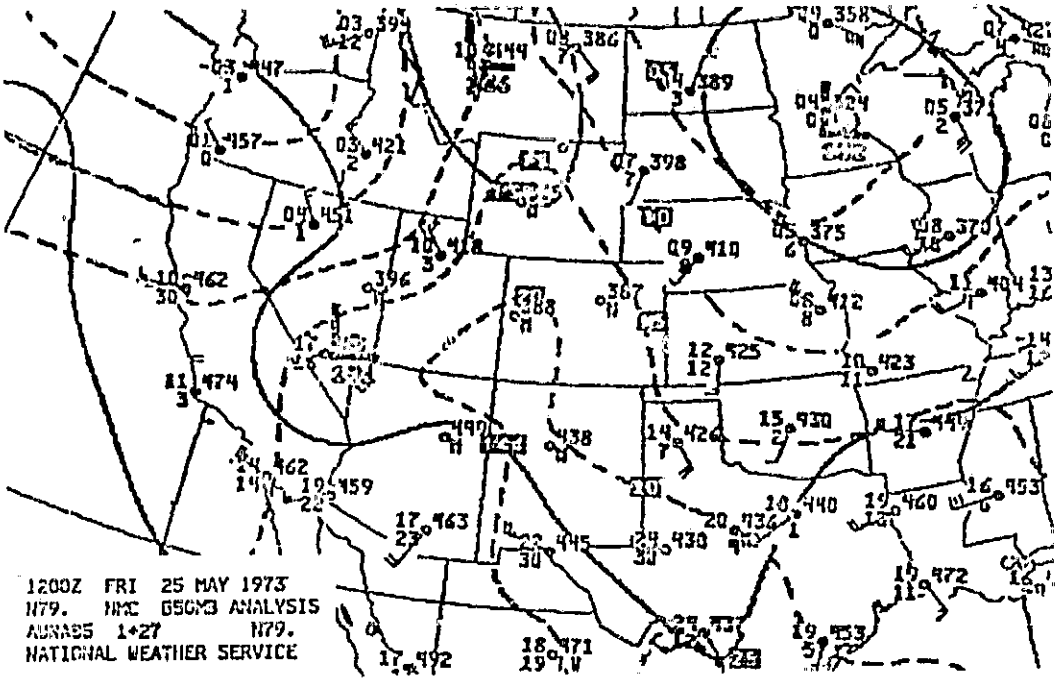

Figure 2a.

Figure 2a-2e. The 850 mb analyses for 25/1200Z to 27/1200Z May 1973 at 12-hour intervals. This series illustrates the warm core nature of the trough in the lee of the mountains. As the system develops, the thermal ridge, which is initially coincident with the trough line, is advected eastward producing strong warm air advection. This is evident in Figures 2b to 2d. The source of the warm air appears to be a combination of radiational heating from the high level terrain of the mountains (Figure 2a), southerly flow, subsiding air over the mountains, and remnants of the warm air of a subsiding ridge (not indicated in these figures). The strong cold air advection to the west of the developing low is associated with frontogenesis.

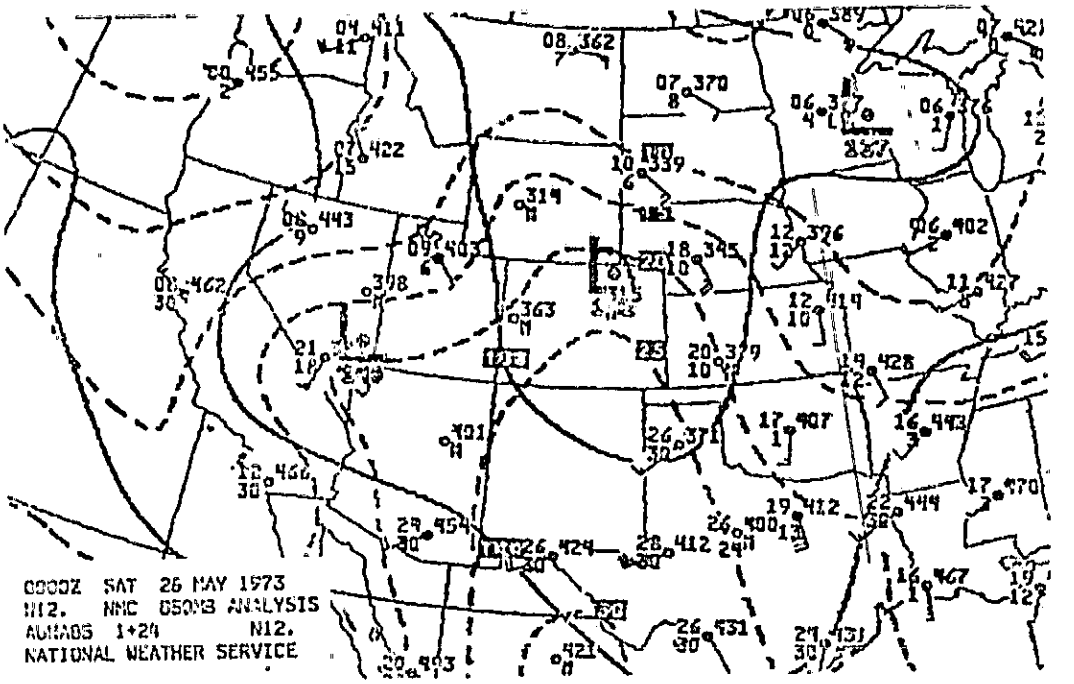

Figure 2b.

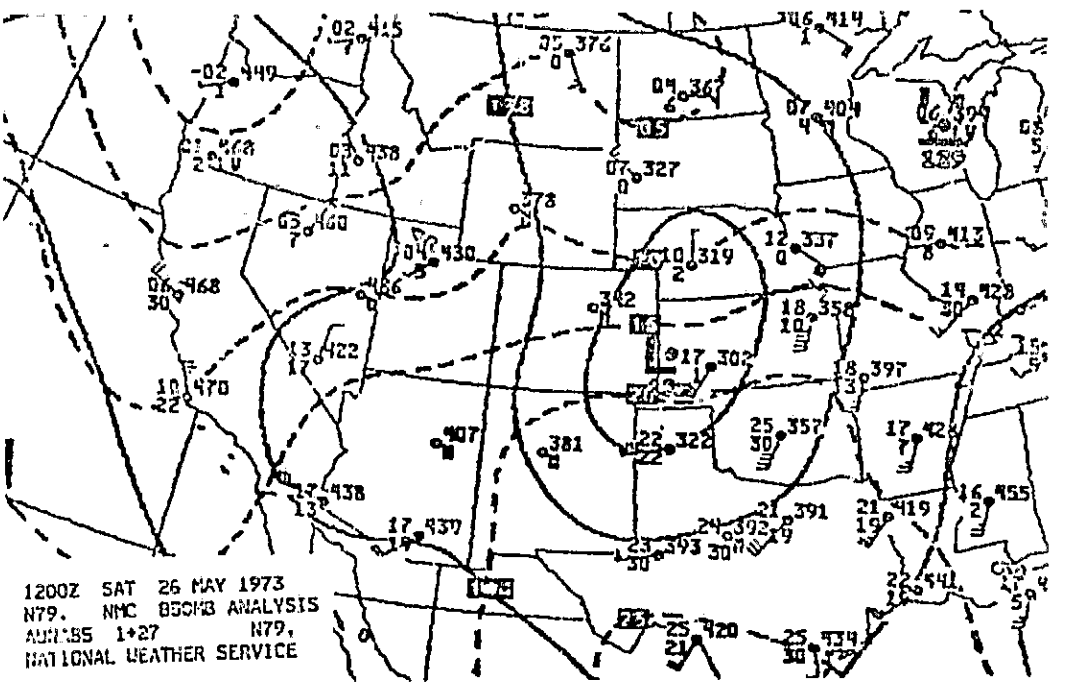

Figure 2c.

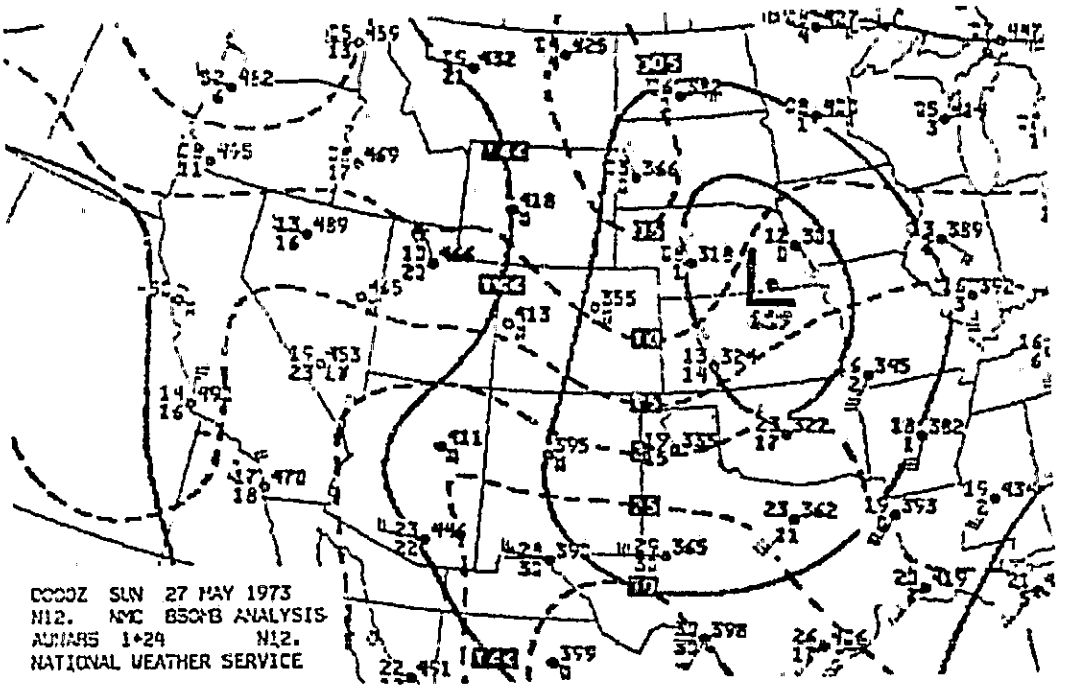

Figure 2d .

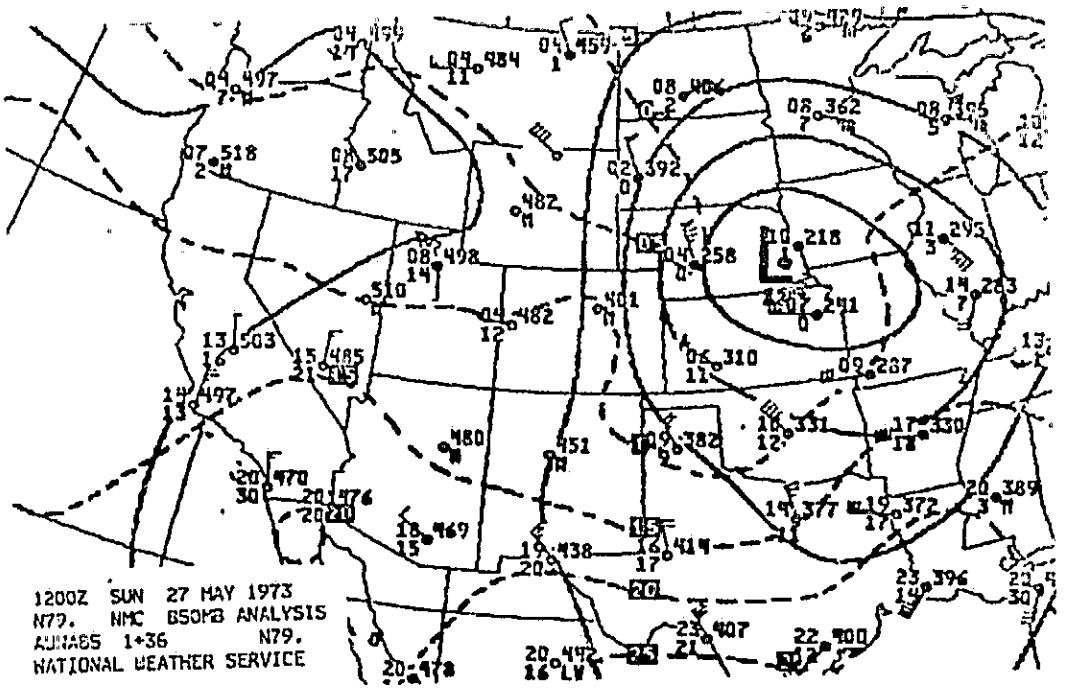

Figure 2 e.

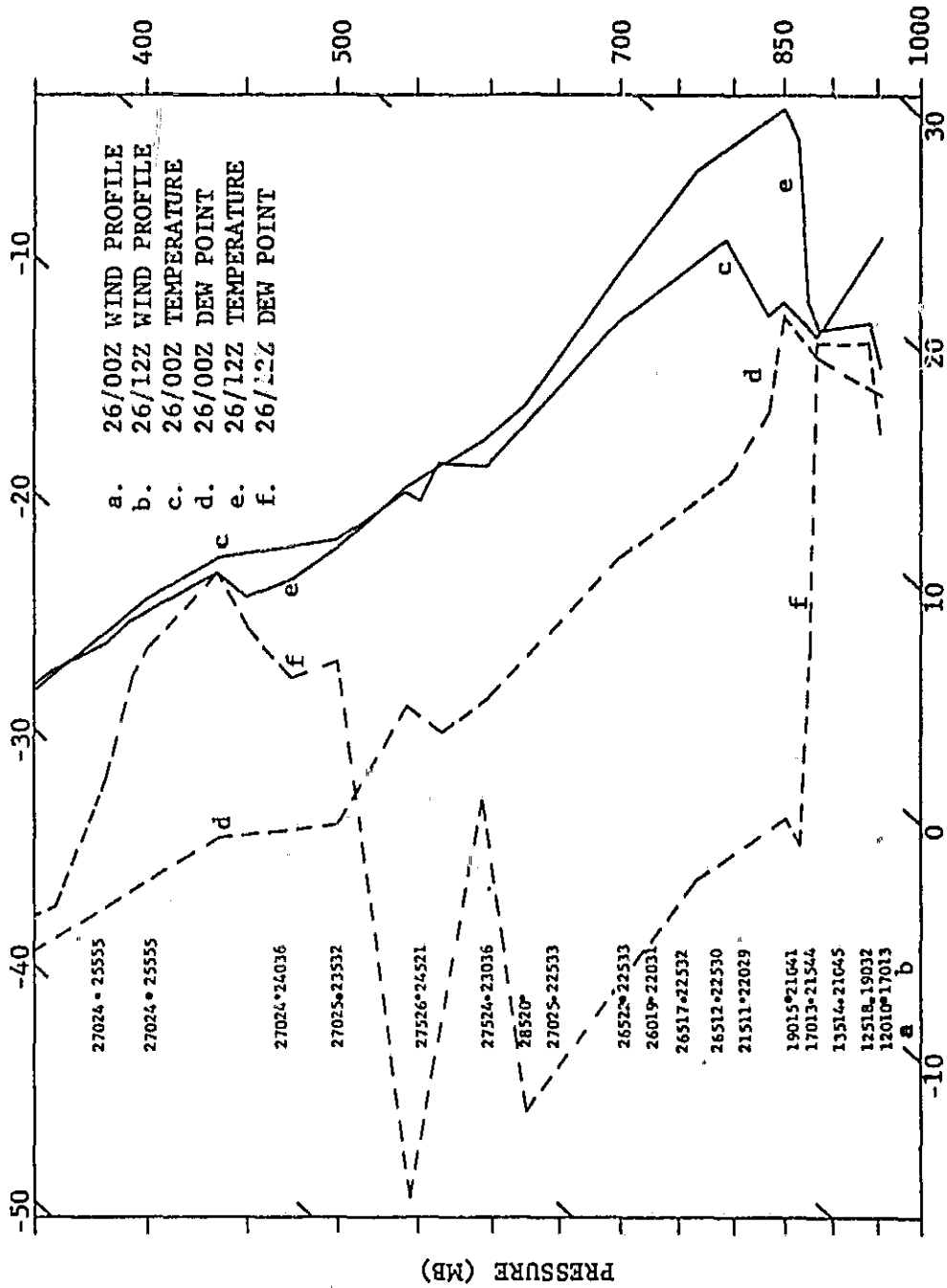

Figure 3. The Tinker AFB, OK (TIK) soundings for 26/00Z and 26/12Z May 1973.

adiabatic lapse rate and strong winds, the vertical and horizontal transport of this temperature is facilitated.

Thus, the analysis of temperature and moisture advection in severe storm environments is a very fruitful area of severe storm research. Studies to date have been hampered by several factors. One factor is the lack of measurements on the meso-scale; another is the accurate computation of the vertical component of motion needed for three dimensional analysis of the advection. It is emphasized that temperature and moisture advection, whether calculated or inferred from the synoptic situation, is a short-range forecast tool. Although advection has a substantial role in the atmosphere (as evidenced by the advection terms in the dynamic models), it cannot describe or account for all the processes which occur. For example, local temperature (thickness) advection will produce accelerations to the wind components as a result of the height gradient changes. This wind change would then affect the advection calculations. Due to these interactions, advection models are short range forecast models. The time span is limited to the order of several hours, the time scale of the thunderstorm and squall line.

The advent of satellite-borne remote sensing offers, through profile inversion techniques based on thermal infrared measurements, the temperature and humidity profiles on scales even smaller than the meso-scale. Two residual problems are that wind measurements still must be derived from other sources and that measurements are contingent upon the availability of the satellite sensors; hence these observations must be time weighted before inclusion in an advection model.

The wind components must, at least for the near future, be derived from the synoptic scale upper air observation network operated by the National Weather Service. The measurement sites are irregularly spaced and the measurements include all scales of motion and contain considerable noise, especially at higher levels and wind speeds (O'Brien, 1970). This noise and the non-resolvable wave lengths in the measurements must be selectively eliminated from the data.

This research is oriented toward the development of an advection model capable of assimilating remotely sensed temperature and moisture profiles (when available) with the temperature, moisture, and wind component data currently available from conventional observations. These data are objectively analyzed using an anisotropic, non-homogeneous weight function designed to minimize errors in the computation of the vertical component of motion. The data are filtered using Sasaki's variational optimization analysis technique to selectively suppress the non-resolvable wavelengths both horizontally and vertically. These assigned data fields are incorporated in a second variational optimization analysis scheme to insure that the advection quantities are continuous within the grid. The final analysis is the correlation of the observed fields and the linear advection of these fields with observed severe thunderstorm environments. This analysis model is a variational optimization analysis model incorporating the time dimension in addition to the three space dimensions. The variational formalism includes filters in the four dimensions to suppress computational error and non-resolvable data field wavelengths introduced at times later than the initialization time.

The severe thunderstorm situation selected for study occurred on 26 May 1973. A prefrontal squall line developed in association with a developing surface low pressure center in southern Kansas. The squall line developed from the Kansas-Oklahoma border southward through eastern Oklahoma. Several tornadoes were reported with this squall line in Kansas and Oklahoma; one tornado in east central Oklahoma claimed five lives in the small town of Keefeton. From Figures 1, 2, and 3, the temperature and moisture advection patterns with the developing system were extensive and pronounced; this research will correlate temperature and advection fields derived from variational optimization analysis methods with the squall line development.

An independent data set was used to develop and verify the numerical models, but the results are not included as a case study. This data set is 11 June 1973; an areal coverage of moderate thunderstorms developed along the Texas-Oklahoma border.

CHAPTER II

DATA OBJECTIVE ANALYSIS

The numeric models of the investigation required an objective analysis to assign values of wind, temperature, and moisture to regularly spaced grid points from the irregularly spaced observation points. The objective analysis method used assigned a grid point value as the weighted average of the surrounding observations; the physical shape of the data fields determines the method of weighting the observed values. The weight function must be carefully selected to avoid unnecessary smoothing of the data fields and to avoid the introduction of frequencies resolvable by the grid network but actually non-resolvable from the observation point network. This may occur when the grid spacing is finer than the average observation point spacing. Filters may be subsequently used to suppress, but not eliminate, the amplitude of non-resolvable wavelengths, as explained in Appendix B. This implies that the assigned data fields be as accurate as possible to avoid the introduction of error into all later numeric aspects of the investigation.

When data to be assigned to regularly spaced grid points from irregularly spaced measurement points are isotropic and homogeneous, the weight functions may be circular and distance dependent. The radius of influence may be determined from the correlation function or from scale considerations if the analytic spectral response of the weight function is known.

However, the horizontal wind components and variables advected by the wind have anisotropic and non-homogeneous correlation functions. A correlation function, as used by Gandin (1965), is the relationship between the correlation coefficients of a data field and distance. The anisotropy stems from a greater correlation parallel to the wind than crosswind. The non-homogeneity arises because the correlations are functions of the wind speed, which varies throughout the grid area. When an isotropic, homogeneous weight function, such as the well-known Cressman function, is used for the objective analysis, errors are introduced into the computations. An example of this is contained as Appendix A, Comparison of Cressman and Anisotropic Exponential Weighting Functions.

An anisotropic, non-homogeneous weighting function was developed for this study. The weight function, W, is defined as

$$W = \frac{V}{V^*} \exp\left\{ \frac{-(x^2 + y^2)}{k(1 + \beta \cos^2 \phi)} \right\}$$

where V = absolute value of the wind speed at the observation point

V^* = defined as a scale maximum wind

$x^2 + y^2$ = distance squared from the observation point to the grid point

k = the filter parameter

β = the anisotropic parameter

ϕ = angle between the wind directional angle and the directional angle from the grid point to the observation point

This weight function was designed by combining the best features of Inman's anisotropic weight function (Inman, 1970) and Barnes' exponential weight function (Barnes, 1973). The exponential form is preferred over the basic Cressman form due to the following desirable

features cited by Barnes:

1. The weight function characteristics can be chosen prior to the analysis so that pattern scales supported by the data distribution will be revealed.

2. Because the weight function approaches zero asymptotically, the influence of data can be extended any distance without changing the weight function and, therefore, the response characteristics. This feature, when compared to the Cressman weight function which has a relatively sharp cut-off at the specified maximum influence radius, is very desirable from a spectral response standpoint because it reduces the high frequencies associated with any weight function or data window.

3. Small scale irregularities are adequately suppressed, so further smoothing is often not necessary.

4. The resolution after one iteration is comparable to four or more iterations in the Cressman successive correction method.

In Barnes' paper, an analytic response function of the exponential weight function showed k to be a low-pass filter parameter. A small value of k allows high frequencies in the data; a larger value of k suppresses these frequencies. The parameter β allows a greater weight to upwind/downwind observations than for crosswind observations. The characteristics of the weight function for selected values of k and β are contained in Figure 4. For the objective analysis of this investigation, k was assigned a value of 0.5 and β was assigned a value of 4.0 after visual examination of the frequencies present in the analyzed wind, temperature, and moisture fields.

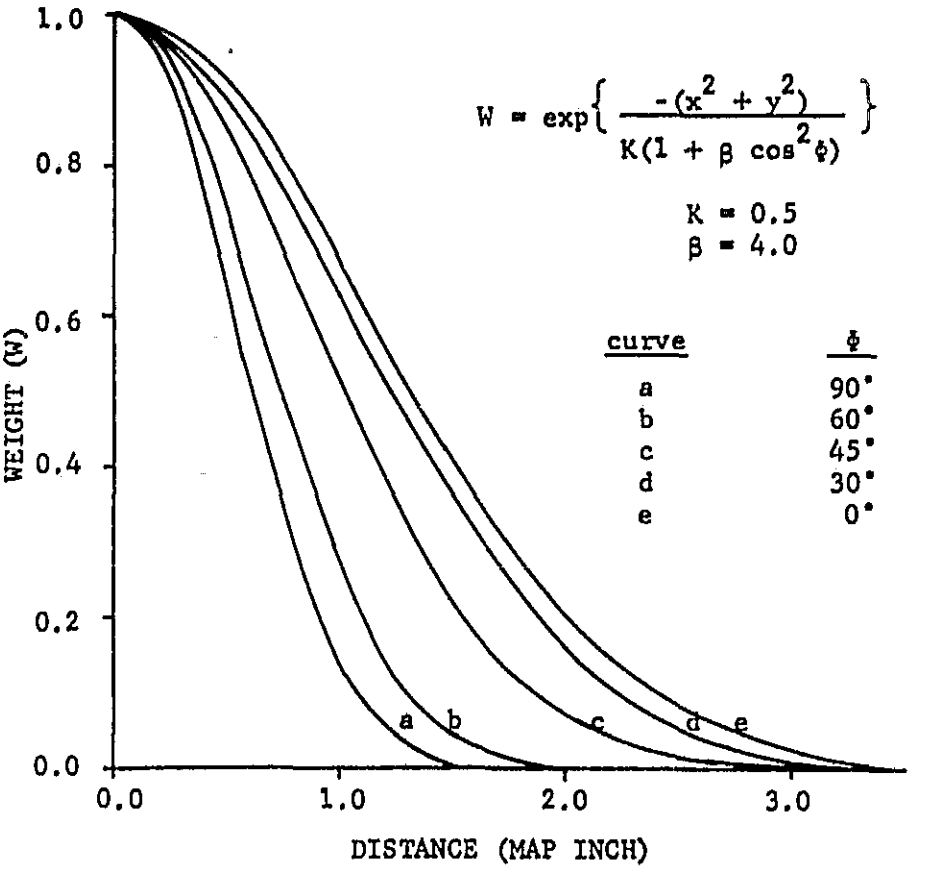

Figure 4. Weight assigned to station observation as a function of distance r, where $r^2 = x^2 + y^2$, and direction vector, ϕ. For the advection investigations, the grid spacing was ½ inch. Note that a family of curves is generated for each set of K and β selected, which governs the degree of anisotropy and scale smoothing.

CHAPTER III

THE VARIATIONAL FILTER

The assigned fields of temperature, moisture, and horizontal wind components require additional filtering to suppress non-resolvable spatial frequencies. The major requirement for filtering arises from the three dimensional nature of the investigation; the initialized data fields have been smoothed implicitly by the weighted average of the observed data points in the horizontal only, and this smoothing has not been uniform due to the anisotropy and inhomogeneity of the weighting function.

Since the upper air reporting network has an average spacing of approximately 400 km over the area of the study, the minimum resolvable wavelength is 800 km under optimal conditions. In the vertical however, wind, temperature, and moisture data are available every 50 mb, the vertical minimum resolvable wavelength is 100 mb. With a computational grid spacing of 125 km horizontally and 50 mb vertically, wavelengths of less than seven horizontal grid units and two vertical grid units should be suppressed.

A filter based on Sasaki's variational optimization analysis technique (Sasaki, 1970a, 1970b, 1971a; Wagner, 1971) is used because the filter characteristics may be specified individually in the horizontal and vertical and applied simultaneously. The variational formalism is

$$\delta J = 0 = \delta \iiint [\tilde{\alpha}[(u-\tilde{u})^2 + (v-\tilde{v})^2] + \alpha_f[(\frac{\partial u}{\partial x})^2 + (\frac{\partial u}{\partial y})^2 + (\frac{\partial v}{\partial x})^2 + (\frac{\partial v}{\partial y})^2] + \alpha_p[(\frac{\partial u}{\partial p})^2 + (\frac{\partial v}{\partial p})^2]\} \, dp \, dx \, dy \qquad (1)$$

where J is the functional; $\tilde{\alpha}$, α_f, and α_p are the specified weak constraint weights applied to the observational terms and to the first derivative filter terms horizontally and vertically.

The Euler-Lagrange equations derived from equation (1) are:

$$\tilde{\alpha}(u-\tilde{u}) - \alpha_f(\frac{\partial^2 u}{\partial x^2} + \frac{\partial^2 u}{\partial y^2}) - \alpha_p \frac{\partial^2 u}{\partial p^2} = 0 \qquad (2a)$$

$$\tilde{\alpha}(v-\tilde{v}) - \alpha_f(\frac{\partial^2 v}{\partial x^2} + \frac{\partial^2 v}{\partial y^2}) - \alpha_p \frac{\partial^2 v}{\partial p^2} = 0 \qquad (2b)$$

These partial differential equations are elliptic and are solved in finite difference form by relaxation techniques. The use of variational optimization analysis in filtering and the derivation of the Euler-Lagrange equations, the solution technique, and the filter response characteristics are contained in Appendix B.

Because sharp gradients on the boundary will introduce error into the interior grids with relaxation techniques, with a resultant decreased convergence rate, the six boundary faces of the three-dimensional grids were filtered before the filtering pass on the interior. The boundary face filtering was accomplished with a two-dimensional variational filter with weak constraint weighting consistent with the weighting used in the interior.

The amount of change in the fields over the 15 x 14 x 18 grid used, expressed as root mean square error (RMSE), for the two investigations is contained in Table 1. As shown, the filtering produced an

average change of less than five percent over the grid network; the maximum changes occurred in the vicinity of sharp gradient changes in the data.

	DATA FIELD			
DATE	$u(m\ sec^{-1})$	$v(m\ sec^{-1})$	θ(deg K)	$w(gms\ kg^{-1})$
11/12Z JUN 73	.4215	.3793	.4046	.0994
26/12Z MAY 73	.4629	.5633	.3976	.1825

TABLE 1. Root mean square error (interior points only) for the three dimensional variational filtering adjustment of the two investigation case studies. The temperature is expressed as potential temperature, θ, and the moisture is expressed as mixing ratio, w.

CHAPTER IV

VERTICAL MOTION COMPUTATION

The variational approach will be also used to calculate the vertical motion and to adjust the entire wind field so that the equation of mass continuity, necessary for advection calculations, is satisfied. The variational method is uniquely able to combine the dynamic constraint of mass continuity with the observational constraint to adjust the wind field such that conservation of advection quantities is assured. This method has been used with success by O'Brien (1970) and McGinley (1973), both based on Sasaki's variational optimization approach. The variational formalism is, in non-dimensional form,

$$\delta J=0=\delta \iiint \{\tilde{\alpha}[(u-\tilde{u})^2 + (v-\tilde{v})^2] + \lambda(\frac{\partial u}{\partial x} + \frac{\partial v}{\partial y} + \frac{\partial \omega}{\partial p})\}dp\ dy\ dx \qquad (3)$$

The resulting Euler-Lagrange equations, derived by carrying out the indicated variations in discrete form and allowing the first variation to be arbitrary in the interior, are

$$2\tilde{\alpha}\ (u-\tilde{u}) - \frac{\partial \lambda}{\partial x} = 0 \qquad (4a)$$

$$2\tilde{\alpha}\ (v-\tilde{v}) - \frac{\partial \lambda}{\partial y} = 0 \qquad (4b)$$

$$- \frac{\partial \lambda}{\partial p} = 0 \qquad (4c)$$

$$\frac{\partial u}{\partial x} + \frac{\partial v}{\partial y} + \frac{\partial \omega}{\partial p} = 0 \qquad (4d)$$

Equations (4a) and (4b) rearranged show that the analyzed fields u and v are derived by adjusting the assigned fields by the gradients of the Lagrange multiplier, λ. As a consequence of equation (4c), λ is independent of pressure.

The Lagrange multiplier field may be determined by the elimination of u and v from equation (4d) by substituion of equation (4a) operated on by $\frac{\partial}{\partial x}$ and equation (4b) operated on by $\frac{\partial}{\partial y}$ to produce

$$\frac{1}{2\tilde{\alpha}} \left(\frac{\partial^2 \lambda}{\partial x^2} + \frac{\partial^2 \lambda}{\partial y^2} \right) = - \left(\frac{\partial \tilde{u}}{\partial x} + \frac{\partial \tilde{v}}{\partial y} \right) - \frac{\partial \omega}{\partial p} \tag{5}$$

This equation may be integrated over pressure to eliminate the term containing ω, since the values of ω may be assigned at the boundaries of the atmosphere. Physically, the vertical motion at the top of the atmosphere is zero; a terrain induced vertical motion may be added at the base (McGinley, 1973). The Lagrange multiplier, λ, is independent of pressure, and the divergence of the observed wind component is known, so λ is calculated from

$$\frac{P_o}{2\tilde{\alpha}} \left(\frac{\partial^2 \lambda}{\partial x^2} + \frac{\partial^2 \lambda}{\partial y^2} \right) = - \int_o^{P_o} \left(\frac{\partial \tilde{u}}{\partial x} + \frac{\partial \tilde{v}}{\partial y} \right) dp \tag{6}$$

where P_o = scaled pressure at base of model. This equation is an elliptic partial differential equation which can be solved for λ by the relaxation technique described in Appendix B. In discrete form, equations (5) and (6) are

$$2\tilde{\alpha}(\nabla_x \tilde{u} + \nabla_y \tilde{v}) + \nabla_x^2 \lambda + \nabla_y^2 \lambda + \nabla_p \omega = 0 \tag{7}$$

$$\frac{P_o}{2\tilde{\alpha}} (\nabla_x^2 \lambda + \nabla_y^2 \lambda) = \sum_P (\nabla_x \tilde{u} + \nabla_y \tilde{v}) \tag{8}$$

In a physical sense, the curvature of the Lagrange multiplier field is proportional to the deviation, or error, from mass continuity of the assigned wind fields. The resulting gradient of λ is then used to adjust the assigned fields of $\tilde{u}$ and $\tilde{v}$ to obtain the analyzed fields as shown by rearranging equations (4a) and (4b) to produce

$$u = \tilde{u} + \frac{1}{2\tilde{\alpha}} \nabla_x \lambda \tag{9a}$$

$$v = \tilde{v} + \frac{1}{2\tilde{\alpha}} \nabla_y \lambda \tag{9b}$$

These analyzed u and v fields may then be used to obtain the analyzed vertical motion field by summation over pressure of equation (4d). The vertical motion, ω, at a specified level, p, is obtained through application of the trapezoidal rule to produce

$$\omega_p = \omega_{p+\Delta p} + \frac{\Delta p}{2} \left[(\nabla_x u + \nabla_y v)_p + (\nabla_x u + \nabla_y v)_{p+\Delta p} \right] \tag{9c}$$

Several interesting results are obtained if mass continuity is treated as a weak constraint rather than a strong constraint. Although mass continuity must still be satisfied in flux calculations, the conversion from continuous to discrete form, the use of a vertical grid axis not necessarily parallel to the pressure axis (of significance with sloping pressure patterns), and the non-exact nature of the boundary conditions for omega will serve to introduce deviations from the calculated mass continuity. Thus, the formalism in discrete form is

$$\delta J = 0 = \sum_{xy} \sum_{p} \tilde{\alpha}(u-\tilde{u})^2 + \tilde{\alpha}(v-\tilde{v})^2 + \beta(\nabla_x u + \nabla_y v + \nabla_p \omega)^2 \tag{10}$$

The Euler-Lagrange equations are

$$\tilde{\alpha}(u-\tilde{u}) - \beta\nabla_x(\nabla_x u + \nabla_y v + \nabla_p \omega) = 0 \qquad (11a)$$

$$\tilde{\alpha}(v-\tilde{v}) - \beta\nabla_y(\nabla_x u + \nabla_y v + \nabla_p \omega) = 0 \qquad (11b)$$

$$\beta\nabla_p(\nabla_x u + \nabla_y v + \nabla_p \omega) = 0 \qquad (11c)$$

From equation (11c), the deviation from zero of mass-continuity is not a function of the pressure.

If equation (11a) is operated on by ∇_y and equation (11b) is operated on by ∇_x and then subtracted from equation (11a), the following result is obtained

$$\nabla_y(u-\tilde{u}) - \nabla_x(v-\tilde{v}) = 0$$

or, rearranged

$$\nabla_x\tilde{v} - \nabla_y\tilde{u} = \nabla_x v - \nabla_y u \qquad (12)$$

or (the same result is readily obtained from equations (9a) and (9b)),

$$\tilde{\zeta} = \zeta \qquad (13)$$

Thus, the relative vorticity, $\tilde{\zeta}$, of the analyzed field is identical to the relative vorticity of the initial field, ζ, which implies that corrections made to the initial wind fields are applied only to the divergent component; the rotational component remains unchanged. This was verified in both case study investigations. With the 500 mb relative vorticity values scaled by multiplying by 10^5, the root mean square errors were of the order 10^{-5}. Printouts of the relative vorticity fields before adjustment and after adjustment at ten levels for both case study investigations confirmed this. This very desirable feature is ordinarily assumed as a consequence of the orthogonality of the rotational and divergent components of the wind fields (O'Brien, 1970 and

Fankhauser, 1974).

Solution of equations (11a-11c) is facilitated by defining a variable

$$\Phi = \nabla_x u + \nabla_y v + \nabla_p \omega \tag{14}$$

and rewriting the equations as

$$\tilde{\alpha}(u-\tilde{u}) - \beta \nabla_x \Phi = 0 \tag{15a}$$

$$\tilde{\alpha}(v-\tilde{v}) - \beta \nabla_y \Phi = 0 \tag{15b}$$

$$\nabla_p \Phi = 0 \tag{15c}$$

The variables u and v can be eliminated from equation (14) by substituting equation (15a) operated on by ∇_x and equation (15b) operated on by ∇_y to produce

$$\Phi = \nabla_x \tilde{u} + \nabla_y \tilde{v} + \frac{\beta}{\tilde{\alpha}} (\nabla_x^2 \Phi + \nabla_y^2 \Phi) + \nabla_p \omega \tag{16}$$

The omega term is eliminated as an unknown by summing equation (16) over pressure. Since Φ is not a function of pressure, the analysis equation

$$\frac{\beta P_o}{\tilde{\alpha}} (\nabla_x^2 \Phi + \nabla_y^2 \Phi) - P_o \Phi = \sum_p (\nabla_x \tilde{u} + \nabla_y \tilde{v}) \tag{17}$$

is an elliptic partial differential equation, very similar to equation (8) (especially for very large values of R), which is solved by relaxation techniques (initial Φ is zero). The resulting field of Φ is then used to adjust the $\tilde{U}$ and $\tilde{V}$ fields in equations (15a) and (15b). The vertical motion field is derived from equation (14).

When mass continuity is a strong constraint, the adjustment of the $\tilde{u}$ and $\tilde{v}$ fields must be accomplished through several iterations through the adjustment process due to the non-exact nature of the center

space finite difference approximations to the first derivatives used to evaluate the divergence and the gradients of λ. For both case study investigations, convergence of the adjusted u and v fields to the continuity satisfied u and v fields was rapid; ten iterations were used.

CHAPTER V

VARIATIONAL OPTIMIZATION ADVECTION ANALYSIS

The analysis of temperature and moisture advection in thunderstorm environments can be accomplished with the advection equations, assuming dry adiabatic processes. These equations are

$$\frac{d\theta}{dt} = 0 = \frac{\partial\theta}{\partial t} + u\,\frac{\partial\theta}{\partial x} + v\,\frac{\partial\theta}{\partial y} + \omega\,\frac{\partial\theta}{\partial p} \tag{18a}$$

$$\frac{dw}{dt} = 0 = \frac{\partial w}{\partial t} + u\,\frac{\partial w}{\partial x} + v\,\frac{\partial w}{\partial y} + \omega\,\frac{\partial w}{\partial p} \tag{18b}$$

The temperature is expressed as potential temperature, θ, through Poisson's equation (Hess, 1959)

$$\theta = T\,(1000/p)^{R_d/C_p} \tag{19}$$

where R_d/C_p, the ratio of the gas constant for dry air to the specific heat of air at constant pressure, is equal to 2/7 and p is the pressure. The moisture is expressed as mixing ratio, w, through the conversion of dew point temperature, T_d, to vapor pressure, e, through Tetens empirical formula (Saucier, 1955)

$$e = 6.108 \exp\{17.27\ T_d\ /\ (237.3 + T_d)\} \tag{20a}$$

and the conversion of vapor pressure to mixing ratio by

$$w = \frac{622\ e}{p - e} \tag{20b}$$

where p is the pressure level, e is the vapor pressure in millibars and

w is the mixing ratio in grams water vapor per kilogram dry air.

These advection equations are often applied diagnostically to determine advection fields, such as horizontal temperature advection for vertical motion analysis. Since these equations contain a time derivative, they are also used in prognostic form; the local time change is evaluated at each grid point and added to the initial value to produce a forecast. A major problem with the use of the advection equation in prognostic form is that discontinuities appear in the forecast field, even when the wind field satisfies mass continuity. Variable propagation speeds, i.e., the wind components, will increase the amount of discontinuity present.

Computational instability is another major problem with the use of the advection equations as prognostic equations. When an advection equation is expressed in center time, center space finite difference approximation form in the x-t plane, the computational form is

$$\tfrac{1}{2}(\phi_{x,t+1} - \phi_{x,t-1}) = \frac{u_{x,t}\Delta t}{\Delta x}\left[\tfrac{1}{2}(\phi_{x+1,t} - \phi_{x-1,t})\right] \qquad (21)$$

where ϕ is the field to be advected, Δt is the time interval, Δx is the grid distance, and u is the propagation speed. As discussed in Haltiner (1971), this form is computationally stable for values of $u\,\Delta t/\Delta x$ less than one. When u is a variable propagation speed, the stability criterion must be satisfield for the maximum speeds in the grid. With y and p grid dimension added, the stability criterion value of one for the coefficients decreases.

Stability can be defined in terms of the amplification tendency in future time steps of a current time step error term, introduced

through roundoff or truncation error or from error in the data field. The numerical scheme is stable if the amplitude of the error remains the same or decreases; instability arises when the amplitude increases. In two dimensions, the new variable value at a time step contains error from only two dimensions, but with three or four dimensions, the error terms which may have been originally orthogonal accumulate at the new time step value of the variable. Thus the stability criterion value decreases. For an excellent graphical presentation of the propagation of error as a function of the coefficient values, see Ketter and Prawel (1969).

Another form of instability, the computational mode, is a result of the use of center time finite difference approximation in the numerical scheme. After the first time step, normally accomplished with a forward time step (which is always unstable), the value of a variable, ϕ, at the nth time step, ϕ^n, is based on advective changes to ϕ^{n-2}. Thus, the values of ϕ at alternate time steps may diverge. Magata and Nishida (1971) found that this non-linear instability could produce the complete destruction of the advective forecast scheme, but could be controlled with the restart technique. They found in a simple advective numerical experiment that the introduction of a forward time step, the restart, at specified time intervals in the forecast scheme would control this instability.

A final problem with the use of the advection equation as a forecast is that new observational data cannot be incorporated into the grid without producing sharp gradients which then dominate the advective scheme. The advective forecast scheme is limited to synoptic

data fields; data available from remote sensing at later times but before the next synoptic observation time cannot be incorporated.

The problems of discontinuities in the advection fields and the inability to update the observational data lead to the formulation of the temperature and moisture advection in storm environments in variational optimization analysis form.

For a purely advective model, the functional is established as

$$J = \iiiint \{\tilde{\alpha}(\theta-\tilde{\theta})^2 + \tilde{\alpha}(w-\tilde{w})^2 + \alpha_1(\frac{d\theta}{dt})^2 + \alpha_1(\frac{dw}{dt})^2\}dt\,dp\,dy\,dx \quad (22)$$

The terms represent the observational constraints and the advection constraints for potential temperature and mixing ratio. In this form, both θ and $\tilde{\theta}$ are functions of time, so new data can be incorporated into the advective process at any time by adjusting the appropriate $\tilde{\theta}$ terms.

The propagation speeds of the advection equations are the continuity satisfied wind components to insure that there are no advection sinks or sources within the field. Through this requirement for mass continuity, the wind component fields will not vary with time at the grid points (this can be established in a functional with observational constraints on the wind components and with the local time change included as either a weak or strong constraint). The wind components remain variable with respect to the spatial derivatives and thus take part in the variations with interesting consequences.

For simplicity, consider a functional similar to equation (22) but for θ in the x-t dimensions only.

$$J = \iint \{\tilde{\alpha}(\theta-\tilde{\theta})^2 + \alpha_1 (\frac{d\theta}{dt})^2\}\, dt\, dx \tag{23}$$

$$\delta J = 0 = \delta \iint [\tilde{\alpha}(\theta-\tilde{\theta})^2 + \alpha_1 (\frac{\partial\theta}{\partial t} + u \frac{\partial\theta}{\partial x})^2]dt\, dx \tag{24}$$

$$0 = \iint \{2\tilde{\alpha}(\theta-\tilde{\theta})\delta\theta + 2\alpha_1 (\frac{\partial\theta}{\partial t} + u \frac{\partial\theta}{\partial x})\ \delta(\frac{\partial\theta}{\partial t} + u \frac{\partial\theta}{\partial x})\}dt\, dx \tag{25}$$

$$= \iint \{2\tilde{\alpha}(\theta-\tilde{\theta})\delta\theta + 2\alpha_1 [\delta\theta(-\frac{\partial}{\partial t}\frac{d\theta}{dt} - \frac{\partial}{\partial x}(u\frac{d\theta}{dt}))]$$

$$+ 2\alpha_1\ \delta u \frac{\partial\theta}{\partial x}\frac{d\theta}{dt}\}\, dt\, dx \tag{26}$$

The Euler-Lagrange equation from the variation of u is

$$2\alpha_1 \frac{\partial\theta}{\partial x}\frac{d\theta}{dt} = 0 \tag{27}$$

Since $\frac{\partial\theta}{\partial x}$ is non-zero, then $d\theta/dt$ is exactly zero, which is analogous to the use of the advection equation as a strong constraint; the local time change of θ is determined solely by advective changes.

The derivation of the Euler-Lagrange equations from equation (22) written for θ is

$$\delta J = 0 = \delta \iiint \{\tilde{\alpha}(\theta-\tilde{\theta})^2 + \alpha_1 (\frac{d\theta}{dt})^2\}\, dt\, dp\, dy\, dx \tag{28}$$

$$= \iiint \{2\tilde{\alpha}(\theta-\tilde{\theta})\delta\theta + 2\alpha_1 \frac{d\theta}{dt}(\frac{\partial\delta\theta}{\partial t} + \delta u \frac{\partial\theta}{\partial x} + u \frac{\partial\delta\theta}{\partial x}$$

$$+ \delta v \frac{\partial\theta}{\partial y} + v \frac{\partial\delta\theta}{\partial y} + \delta\omega \frac{\partial\theta}{\partial p} + \omega \frac{\partial\delta\theta}{\partial p}\}\, dt\, dp\, dy\, dx \tag{29}$$

$$= \iiint [\delta\theta[\tilde{\alpha}(\theta-\tilde{\theta}) - \alpha_1 \frac{\partial}{\partial t}\frac{d\theta}{dt} - \frac{\partial}{\partial x}(u\frac{d\theta}{dt})$$

$$- \frac{\partial}{\partial y}(v\frac{d\theta}{dt}) - \frac{\partial}{\partial p}(\omega\frac{d\theta}{dt})] + \delta u\alpha_1 \frac{\partial\theta}{\partial x}\frac{d\theta}{dt}$$

$$+ \delta v\alpha_1 \frac{\partial\theta}{\partial y}\frac{d\theta}{dt} + \delta\omega\alpha_1 \frac{\partial\theta}{\partial p}\frac{d\theta}{dt}\}\, dt\, dp\, dy\, dx \tag{30}$$

The other problem is the difficulty of numerical solution of this parabolic equation with four dimensions. With the time dimension plus any other spatial dimension, a marching method, common to the numerical solution of parabolic equations, will generate three unknown coefficients at each time step due to the finite difference approximation form of the mixed derivative term. At each time step, a square tridiagonal matrix of these unknown coefficients is generated. When the computational stability criteria are satisfied, the tridiagonal matrix is well-conditioned (dominant diagonal elements) and the coefficients are easily determined by Gauss elimination (Ketter and Prawel, 1969). When other spatial dimensions are added, the numerical solution becomes very complex.

Both of these problem areas can be adequately resolved by the addition of temporal and spatial first derivative filters to the functional (Sasaki, 1971b) to produce (in θ only for simplicity)

$$J = \int\int\int\int \{ \alpha(\theta-\theta)^2 + \alpha_1 \left(\frac{d\theta}{dt} \right)^2 + \beta_1 \left(\frac{\partial\theta}{\partial t} \right)^2 + \beta_2 \left[\left(\frac{\partial\theta}{\partial x} \right)^2 + \left(\frac{\partial\theta}{\partial y} \right)^2 \right] + \beta_3 \left(\frac{\partial\theta}{\partial p} \right)^2 \} dt\, dp\, dy\, dx \qquad (34)$$

The inclusion of the filter terms effectively suppresses the discontinuities, which are high frequency. The solution field of θ is basically an advection field with the discontinuities suppressed. As a very essential additional benefit, the inclusion of the filter terms changes the analysis equations from parabolic partial differential equations to the more tractable elliptic form. The Euler-Lagrange equation from the variation of θ is now

$$\alpha_1\left(\frac{d^2\theta}{dt^2}\right) + \beta_1 \frac{\partial^2\theta}{\partial t^2} + \beta_2\left(\frac{\partial^2\theta}{\partial x^2} + \frac{\partial^2\theta}{\partial y^2}\right) + \beta_3\left(\frac{\partial^2\theta}{\partial p^2}\right) = \tilde{\alpha}(\theta-\tilde{\theta}) \qquad (35)$$

Equation (35) expanded and rearranged forms the analysis equation

$$(\alpha_1+\beta_1)\frac{\partial^2\theta}{\partial t^2} + (\alpha_1 u^2 + \beta_2)\frac{\partial^2\theta}{\partial x^2} + (\alpha_1 v^2 + \beta_2)\frac{\partial^2\theta}{\partial y^2}$$

$$+ (\alpha_1\omega^2 + \beta_3)\frac{\partial^2\theta}{\partial p^2} + 2\alpha_1\left(u\frac{\partial^2\theta}{\partial x\partial t} + v\frac{\partial^2\theta}{\partial y\partial p} + \omega\frac{\partial^2\theta}{\partial p\partial t} + uv\frac{\partial^2\theta}{\partial x\partial y} + u\omega\frac{\partial^2\theta}{\partial x\partial p} + v\omega\frac{\partial^2\theta}{\partial y\partial p}\right)$$

$$+ \alpha_1\left[u\left(\frac{\partial u}{\partial x}\frac{\partial\theta}{\partial x} + \frac{\partial v}{\partial x}\frac{\partial\theta}{\partial y} + \frac{\partial\omega}{\partial x}\frac{\partial\theta}{\partial p}\right) + v\left(\frac{\partial u}{\partial y}\frac{\partial\theta}{\partial x} + \frac{\partial v}{\partial y}\frac{\partial\theta}{\partial y} + \frac{\partial\omega}{\partial y}\frac{\partial\theta}{\partial p}\right) + \omega\left(\frac{\partial u}{\partial p}\frac{\partial\theta}{\partial x} + \frac{\partial v}{\partial p}\frac{\partial\theta}{\partial p} + \frac{\partial\omega}{\partial p}\frac{\partial\theta}{\partial p}\right)\right]$$

$$= \tilde{\alpha}(\theta - \tilde{\theta}) \qquad (36)$$

This equation is an elliptic type partial differential equation, which is solved through relaxation techniques. The type of equation may be verified in any two dimensions by examining the characteristic quadratic form (the familiar $B^2-4AC < 0$). In x and t,

$$4u^2\alpha_1^2 - 4(\alpha_1 + \beta_1)(\beta_2 + \alpha_1 u^2) < 0$$

is satisfied for any positive weights α_1, β_1, and β_2. Note that without the addition of the weights (the filter terms), equation (36) reduces to a parabolic type equation.

$$4u^2\alpha_1^2 - 4u^2\alpha_1^2 = 0$$

Equation (35), a linear partial differential equation with variable coefficients, is the primary analysis equation for the advection of temperature; a comparable equation for moisture is obtained by the

same derivation technique.

The solution of equation (35) requires that the "observed" fields of temperature and mixing ratio be established for all time steps. As a result of the variational optimization analysis, which determines the best fit of a field subject to the constraints imposed, the observed data fields must be as accurate as possible. Accuracy in this sense implies a consistency of the observed fields with the diagnostic and prognostic constraints, although a simultaneous consistency is not possible without using a variational model. This indicates that the observed data fields in time should be determined by advection from the initial time. The result should be a faster convergence (savings on computer time) to more realistic final data fields.

An interesting corollary to this point is that perhaps the most important application of the variational optimization analysis method is to adjust observed data fields to a form consistent with the diagnostic and prognostic equations of the model. The data fields are adjusted using explicitly all available information, which may be statistical, dynamic, kinematic, thermodynamic, or energetic (see, for example, Lewis and Grayson, 1972).

The observed fields at the time steps were determined by the linear advection equations in the form

$$-\frac{\partial \theta}{\partial t} = u\frac{\partial \theta}{\partial x} + v\frac{\partial \theta}{\partial y} + \omega\frac{\partial \theta}{\partial p} \tag{37}$$

In scaled, non-dimensional form using center time and center space finite difference approximations, equation (37) is

$$-\nabla_t \theta = \frac{V^*\Delta t}{\Delta x}\left(u'\nabla_x \theta + v'\nabla_y \theta\right) + \frac{W^*\Delta t}{\Delta p}\,\omega'\nabla_p \theta \tag{38}$$

where $u = u'V^*$, $V^* = 10$ m sec^{-1}

$v = v'V^*$

$\omega = \omega'W^*$, $W^* = 10^{-3}$ mb sec^{-1}

Δx = horizontal grid distance, approximately 1.25×10^5 m

Δp = vertical grid distance, 50 mb

Δt = time grid scale, 600 sec

$\nabla_n \Phi = \frac{1}{2}(\Phi_{n+1} - \Phi_{n-1})$

In view of the variable propagation speeds, the scheme was restarted every two hours (7200 sec) as a precaution to prevent the high frequency computational instability.

CHAPTER VI

RESULTS

With cyclogenesis and frontogenesis in the lee-of-the-mountain trough, temperature and moisture advection patterns from the surface to the 700 millibar level are pronounced, as shown in Figures 1, 2, and 3. From the omega equation, upward motion should be associated with the low level temperature advection and from Miller (1972), storm development should be associated with the moist and dry advection patterns. He states,

> In situations preceding significant tornado development, a distinct dry tongue is present in low or middle levels, and, provided other criteria are satisfied, the primary development will occur where the dry tongue intrudes into or over the lower moist tongue... Dry air intrusions not only help in delineating future tornado and severe weather areas, but apparently provide a major contribution to the trigger mechanism in the majority of tornado situations.

The 26/1200Z May 1973 case study shows that the warm air of the thermal ridge is also very dry; most dew point depressions in the dry air were reported as the maximum reportable 30 degrees Celsius. Several figures emphasize these features and that they are of sufficient horizontal and vertical extent to be resolvable in the advection analysis. Figure 5a shows the pressure and frontal patterns at 26/1200Z May 1973

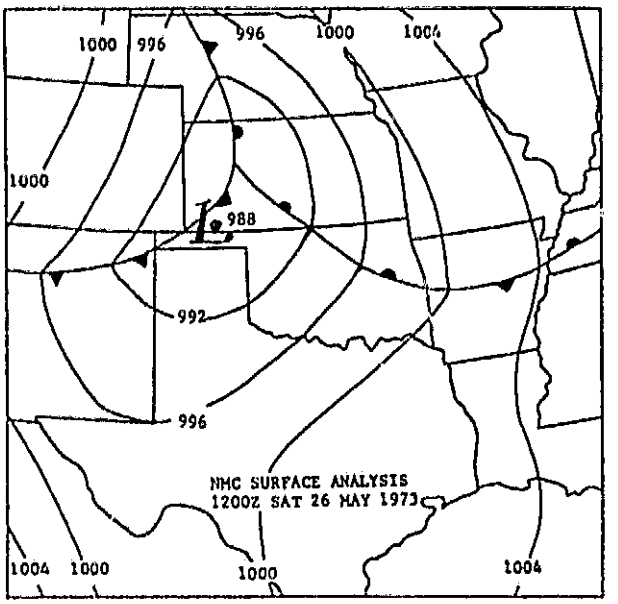

Figure 5a. NMC Surface Analysis, 26/1200Z MAY 1973

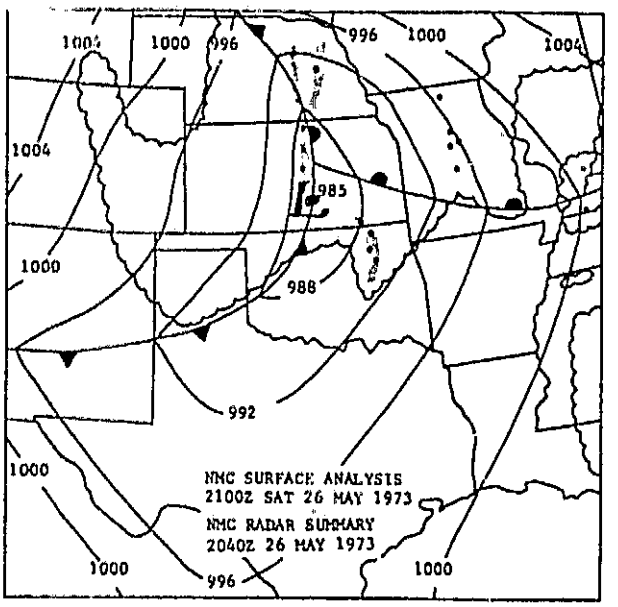

Figure 5b. NMC Surface Analysis, 26/2100Z MAY 1973, and Radar Summary, 26/2040Z MAY 1973. The shaded area indicates thunderstorm line activity; cells with tops over 40,000 ft. are indicated by large dots.

and Figure 5b shows the pressure and frontal patterns at 26/2100Z with the radar detected thunderstorm coverage at 26/2040Z. At 26/1200Z, there were no radar echoes in Oklahoma except along the extreme northern border with Kansas. The prefrontal squall line depicted in Figure 5b originated in north central Oklahoma and developed southward. The radar echo coverage included for reference in succeeding figures is the 26/2140Z thunderstorm activity.

As shown in Figure 3, the warm, dry air lies over cooler, moist air with a very sharp inversion surface at the boundary. Figure 6 shows that this inversion is horizontal over several hundred kilometers extent; the location where this sharp moisture discontinuity intersects the higher terrain of West Texas is known as the dry line, dry front, or Marfa front (from Marfa in southwest Texas). The dry line location at 26/1200Z was between Midland TX and Abilene TX; the Midland dew point temperature was -5 deg C (23 deg F) and the Abilene dew point was 21 deg C (70 deg F). The temperature and dew point profile for these two stations is shown in Figure 7; the moist layer at Abilene is shallow. The high dew point temperature at Abilene is part of the surface layer moisture ridge, which is shown in Figure 8.

The advection analysis grid was a 11 by 10 by 18; the grid spacing was near 125 km horizontally and 50 mb vertically. Twelve time steps were used in the four dimensional advection analysis; the time interval was 20 minutes. The actual wind speeds were used as the advective propagation speeds. The horizontal grid network is shown in Figure 9.

The continuity satisfied vertical motion field at 26/12Z

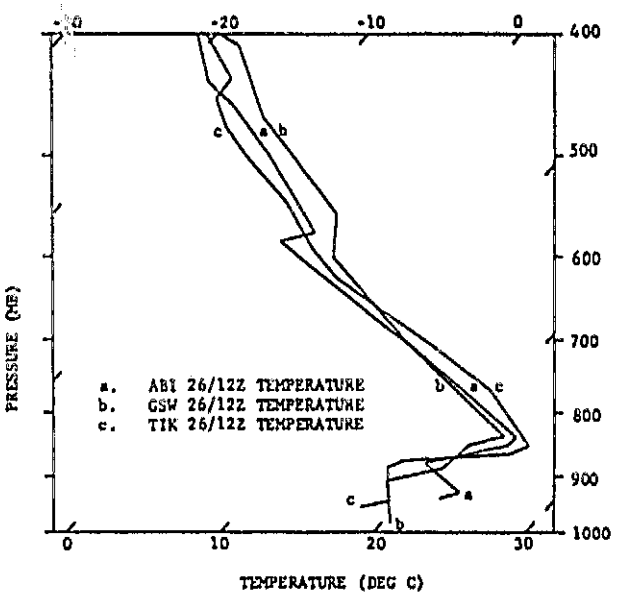

Figure 6. Temperature profiles for Abilene TX (ABI), Greater Southwest Airport TX (GSW), and Tinker AFB OK (TIK) 26/1200Z May 1973.

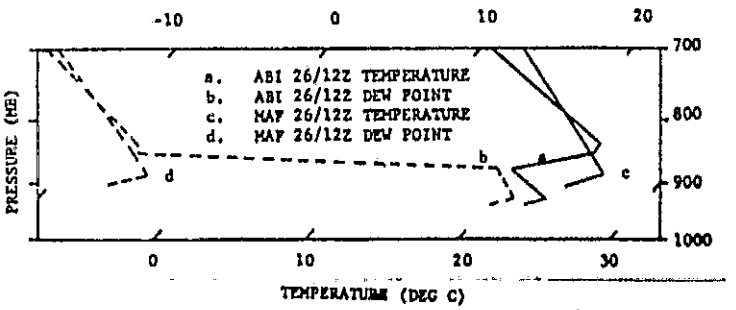

Figure 7. Temperature and dew point temperature profiles for Abilene TX (ABI) and Midland TX (MAF), 26/1200Z May 1973. The surface dew point at Midland is -5 deg C (23 deg F) and at Abilene is 21 deg C (70 deg F).

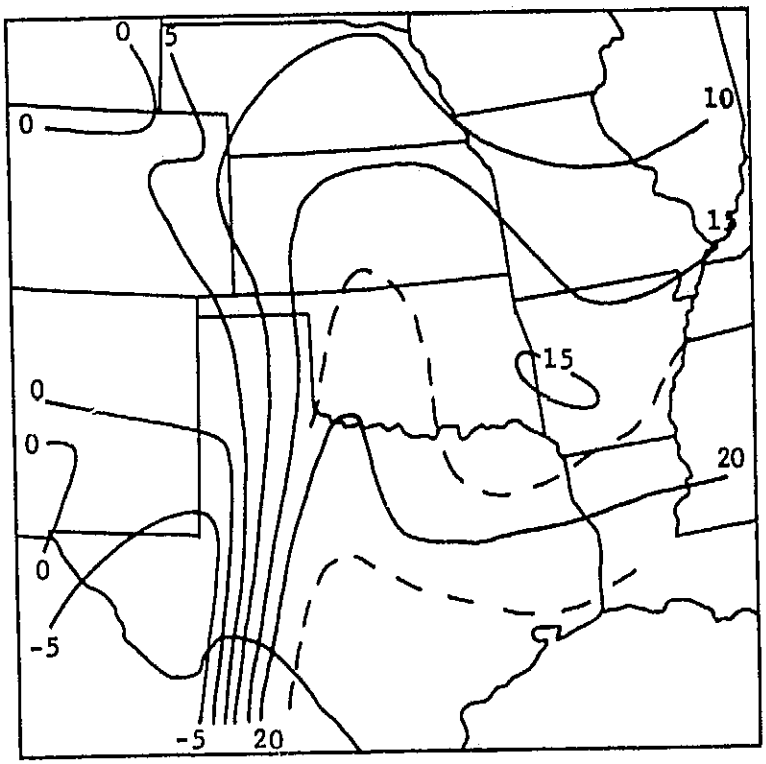

Figure 8. The dew point temperature at 26/1200Z May 1973. The sharp gradient in western Texas represents the dry line.

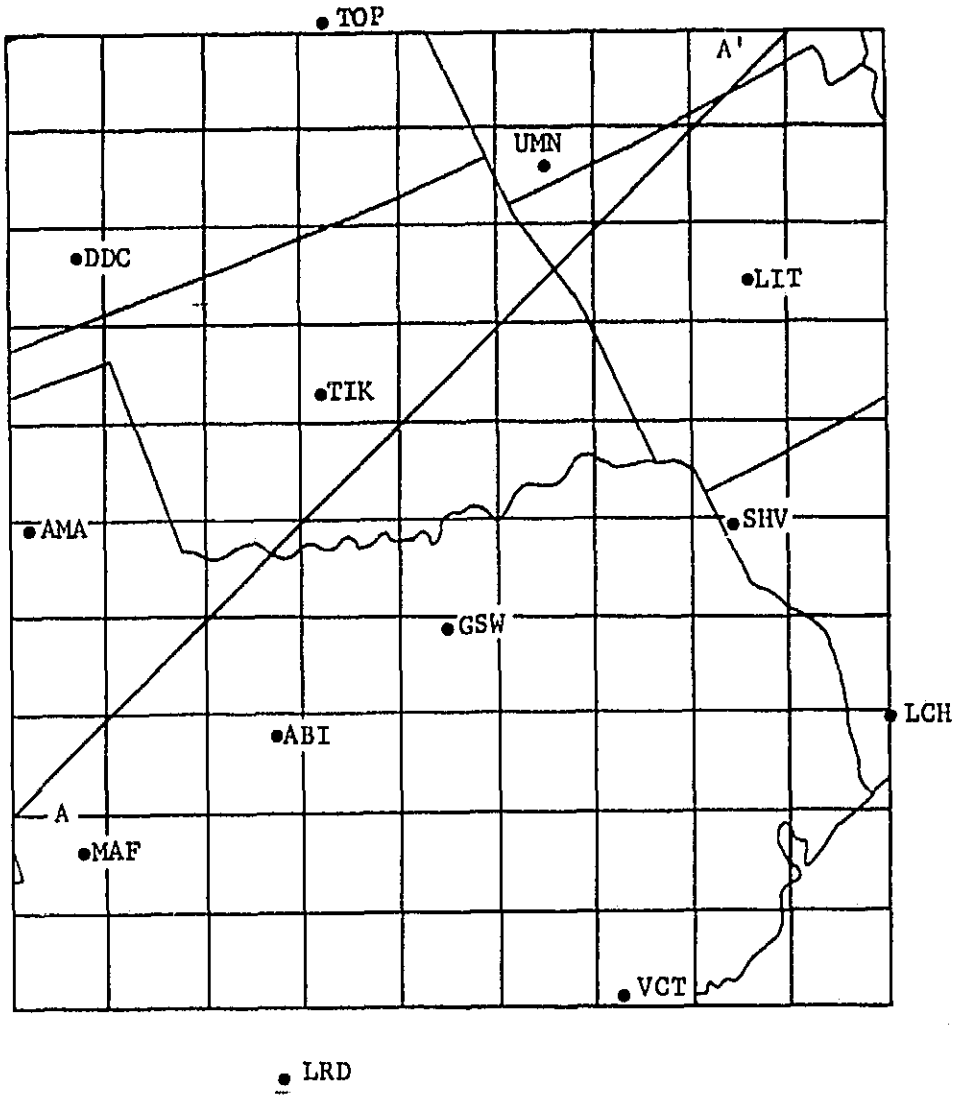

Figure 9. The 11 x 10 horizontal grid established for the advection analysis. The vertical grid has 18 levels at 50 mb intervals; the horizontal grid spacing is near 125 km. Section A-A' is the cross section used in the 26/1200Z MAY 1973 analysis.

contained several features of interest. The omega fields at the 900, 800, 700, 600, and 500 millibar levels are in Figure 10. The axis of maximum upward vertical motions (negative ω) coincides with the area of maximum temperature advection apparent in Figure 1b and 2c. This axis also bears a strong similarity to the squall line location. A secondary axis of upward vertical motion is parallel to the frontal thunderstorm development. This is most evident at the 700 millibar level. At the 500 millibar level, an area of downward vertical motion appears through central Oklahoma. Downward motion behind a squall line has been proposed as a compensatory motion which transfers the higher wind speeds to lower levels (Miller, 1972); the appearance of this downward motion may be purely coincidental, although it does occur in these data before squall line initiation.

The vertical motion in the cross-section along line A-A' (see Figure 9) perpendicular to the squall line axis shows that the downward vertical motion at the 500 millibar level is part of an organized circulation, illustrated in Figure 11. The nature of this potentially very significant circulation pattern will have to be verified in other case studies; perhaps the downward motion is a compensating motion for the upward motion associated with the warm air advection at lower levels. This would produce warming and drying with the subsiding air, which could then enhance the warm, dry intrusion.

The existing temperature and moisture advection fields were calculated at 26/1200Z from the advection equations

$$\frac{\partial \theta}{\partial t} = - \left(u \frac{\partial \theta}{\partial x} + v \frac{\partial \theta}{\partial y} + \omega \frac{\partial \theta}{\partial p} \right) \tag{39a}$$

$$\frac{\partial w}{\partial t} = - \left(u \frac{\partial w}{\partial x} + v \frac{\partial w}{\partial y} + \omega \frac{\partial w}{\partial p} \right) \tag{39b}$$

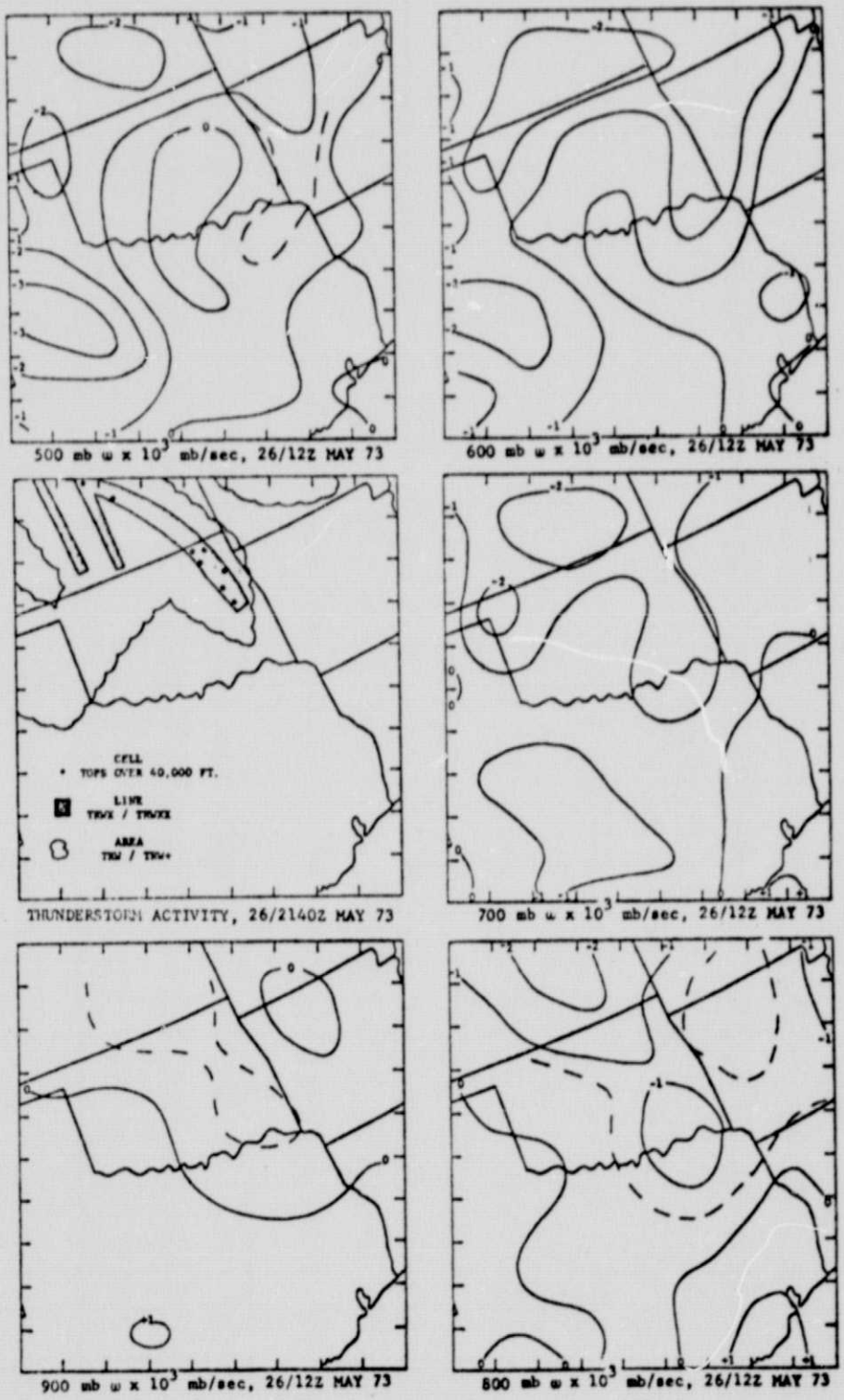

Figure 10. Vertical motion, $\omega \times 10^3$ mb/sec, at 26/1200Z May 1973. The radar summary at 26/2140Z May 1973 is included for reference.

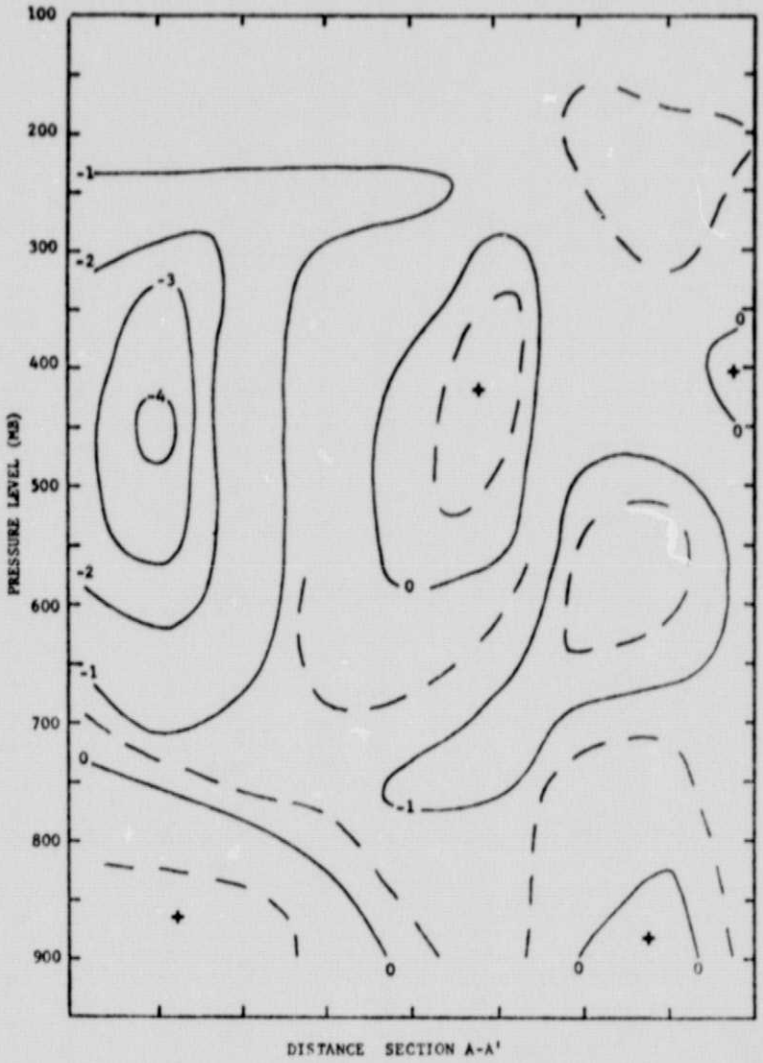

Figure 11. Vertical motion, $\omega \times 10^3$ mb/sec, along the cross section A-A'. The downward motion areas (positive ω) are indicated by the symbol +.

These advective fields, Figure 12 and 13, show that the maximum temperature advection is positively correlated with the maximum drying. The axes of the maximum drying and maximum warming are both parallel to the squall line, as anticipated by application of Miller's (1972) empirical rules. Figure 13 also illustrates the low level moisture increase at the 900 millibar level beneath the drying associated with the warm, dry intrusion. This pattern is more pronounced in cross-section in Figure 14, which includes the 950 millibar level advective fields. The moisture increase at low level on the left hand side of the section is associated with the moisture advection from the moisture ridge depicted in Figure 8. The low level temperature advection fields are weak beneath the warm intrusion, as shown in cross section in Figure 15.

The advective fields computed from the forecast potential temperature and mixing ratio fields show the continued development of the patterns Miller cites as necessary for severe storm development, as shown in Figures 16, 17, 18, and 19. The advective patterns reflect moisture advection below the warm, dry intrusion, which is being advected eastward. This is coincident with continued weak moist advection above the dry intrusion, not shown in these figures but evident from Figure 3. This pattern is cited by Miller as a possible trigger mechanism for the squall line initiation, as shown in Figure 20. The temperature advection pattern shows the strengthening of the mid-level cooling behind the intrusion and continued warm advection with the intrusion.

As suggested by Miller and as indicated by the results of the advection model (Figures 12 and 16), the severe thunderstorms initially develop through the warm, dry inversion layer. Further evidence of this is contained in the ATS-III imagery of 26 May 1973. The ATS III imagery and possible interactions of the mesoscale warm, dry intrusion and the thunderstorm scale processes are discussed in Appendix C.

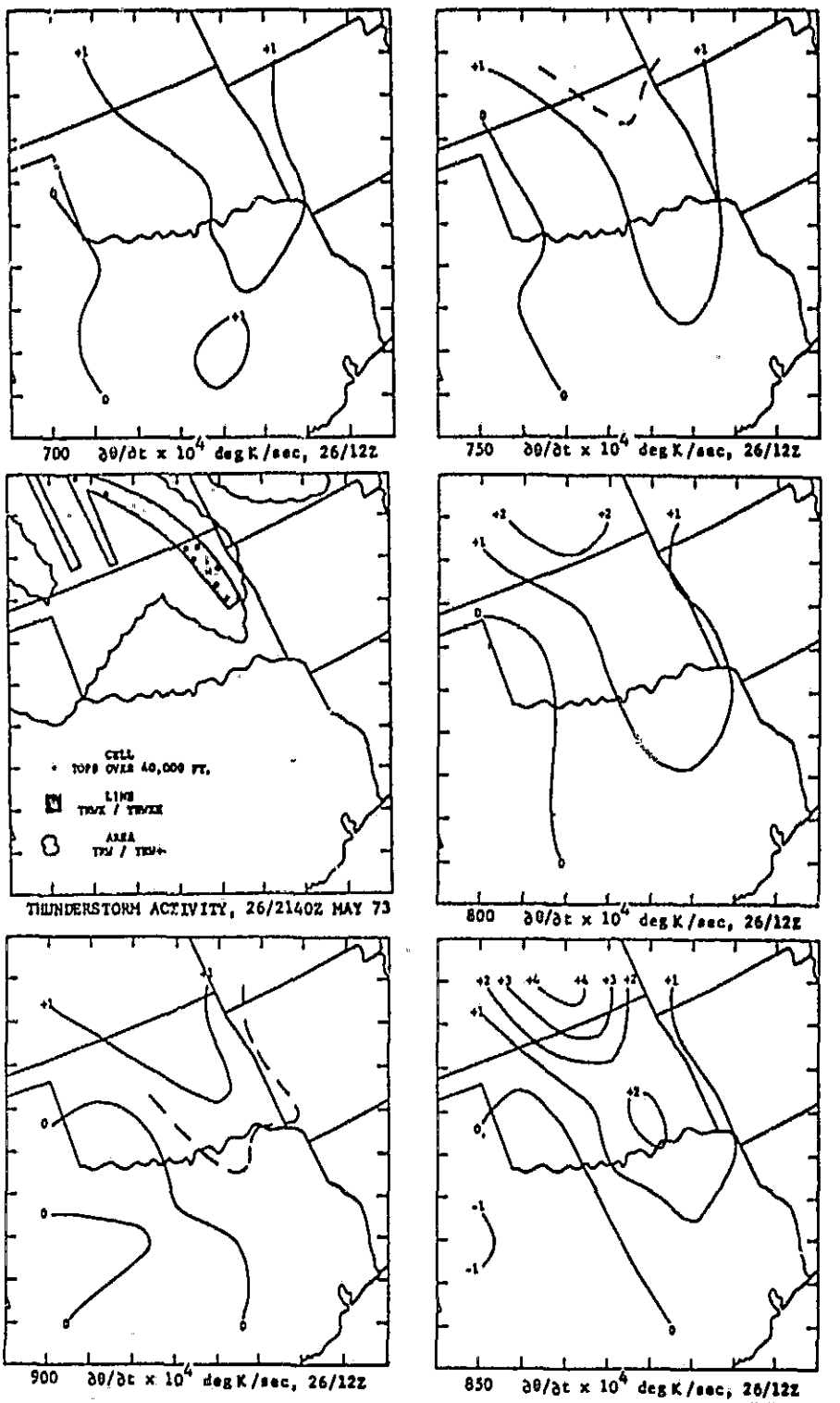

Figure 12. The local change of potential temperature, $\partial\theta/\partial t \times 10^4$ deg K/sec, at 26/1200Z May 1973.

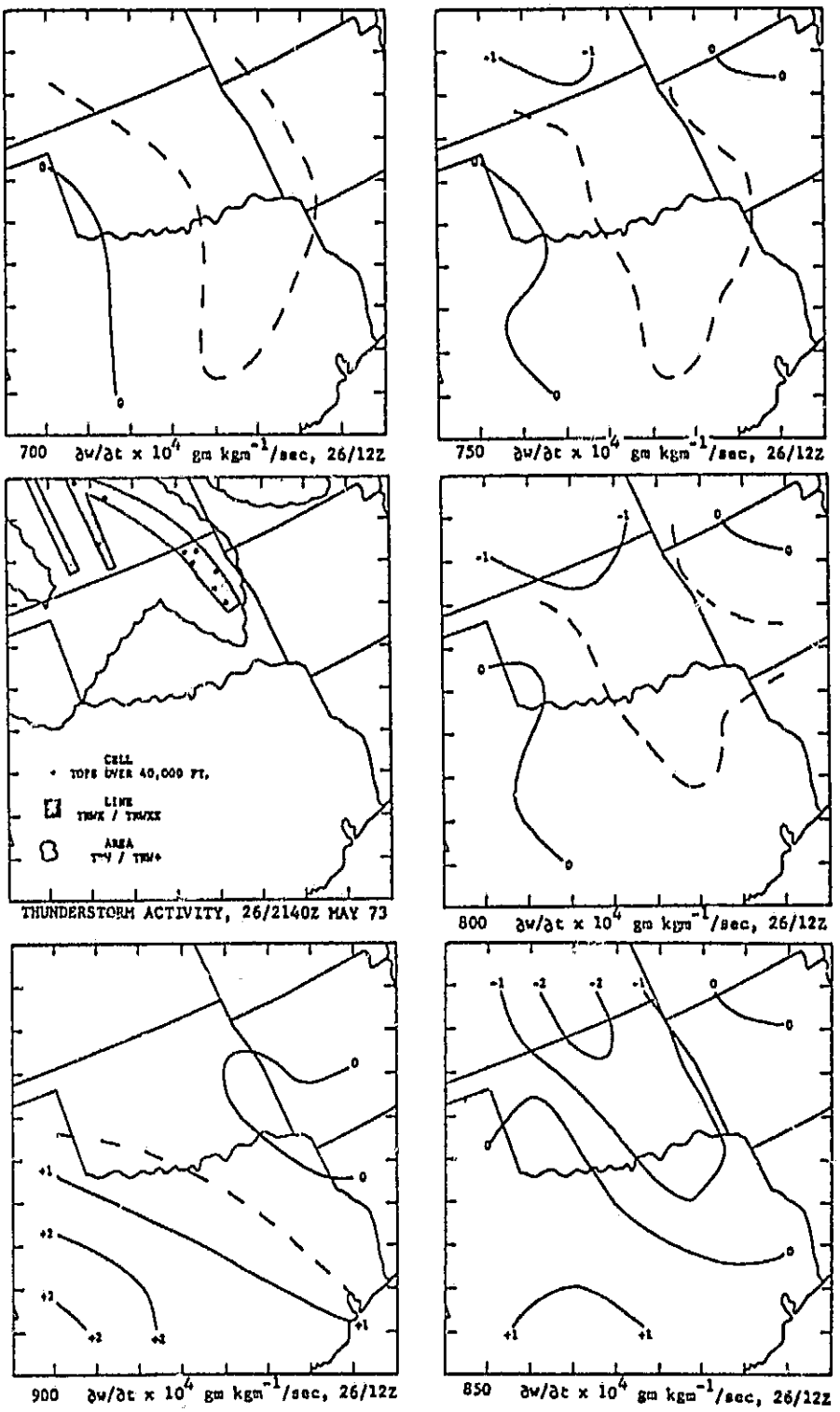

Figure 13. The local change of mixing ratio, $\partial w/\partial t$ x 10^4 gm kgm^{-1}/sec, at 26/1200Z May 1973.

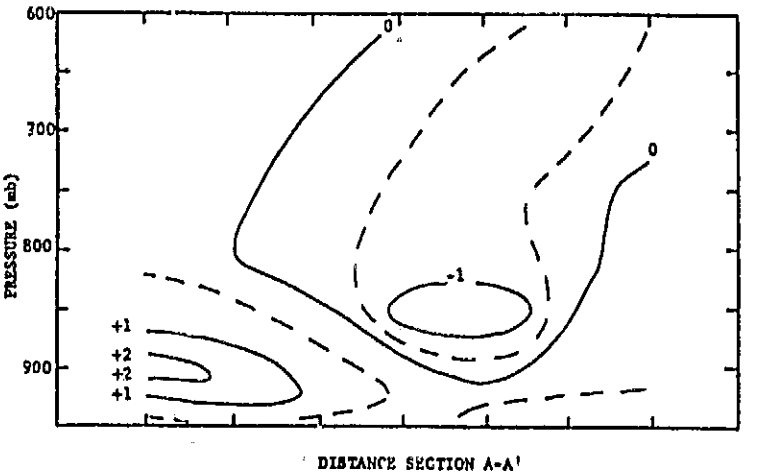

Figure 14. The local change of mixing ratio, $\partial w/\partial t$ x 10^4 gm kgm^{-1}/sec, for the cross-section A-A', 26/1200Z May 1973.

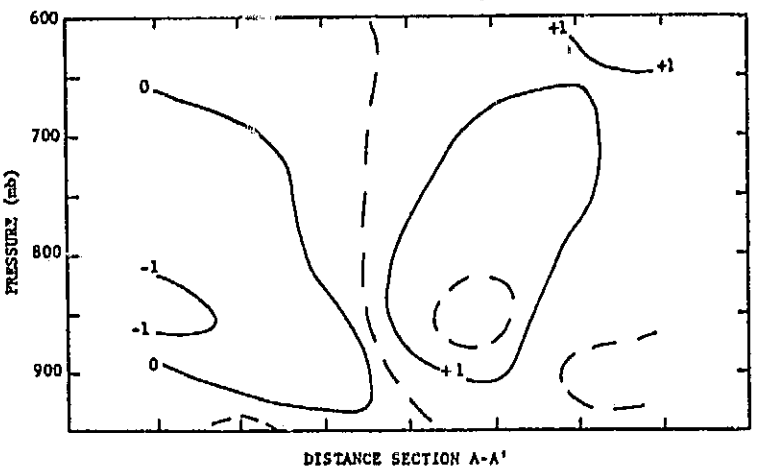

Figure 15. The local change of potential temperature, $\partial\theta/\partial t$ x 10^4 deg K/sec, for the cross-section A-A', 26/1200Z May 1973.

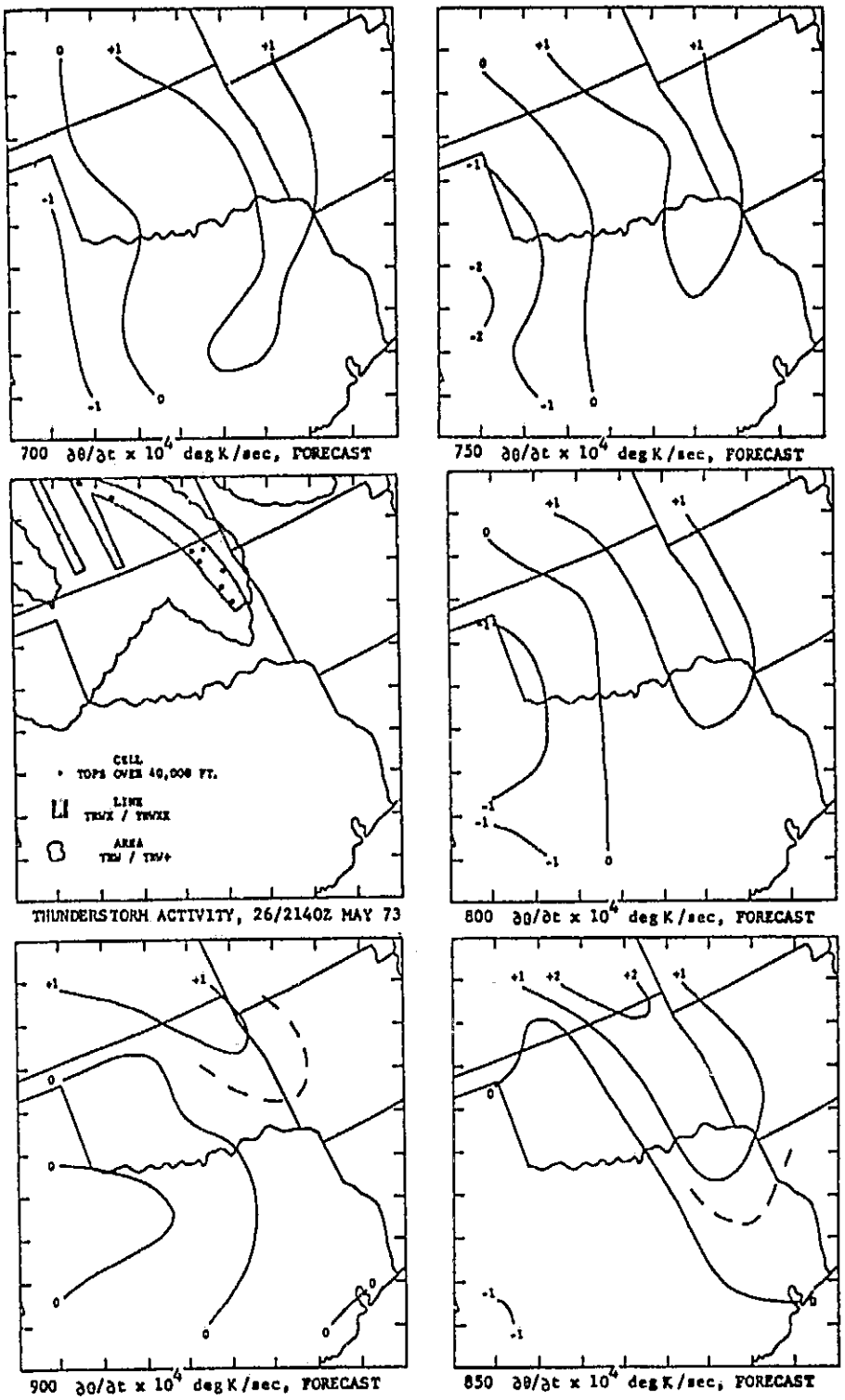

Figure 16. The local change of potential temperature, $\partial\theta/\partial t \times 10^4$ deg K/sec, at the advective forecast time 26/1520Z May 1973.

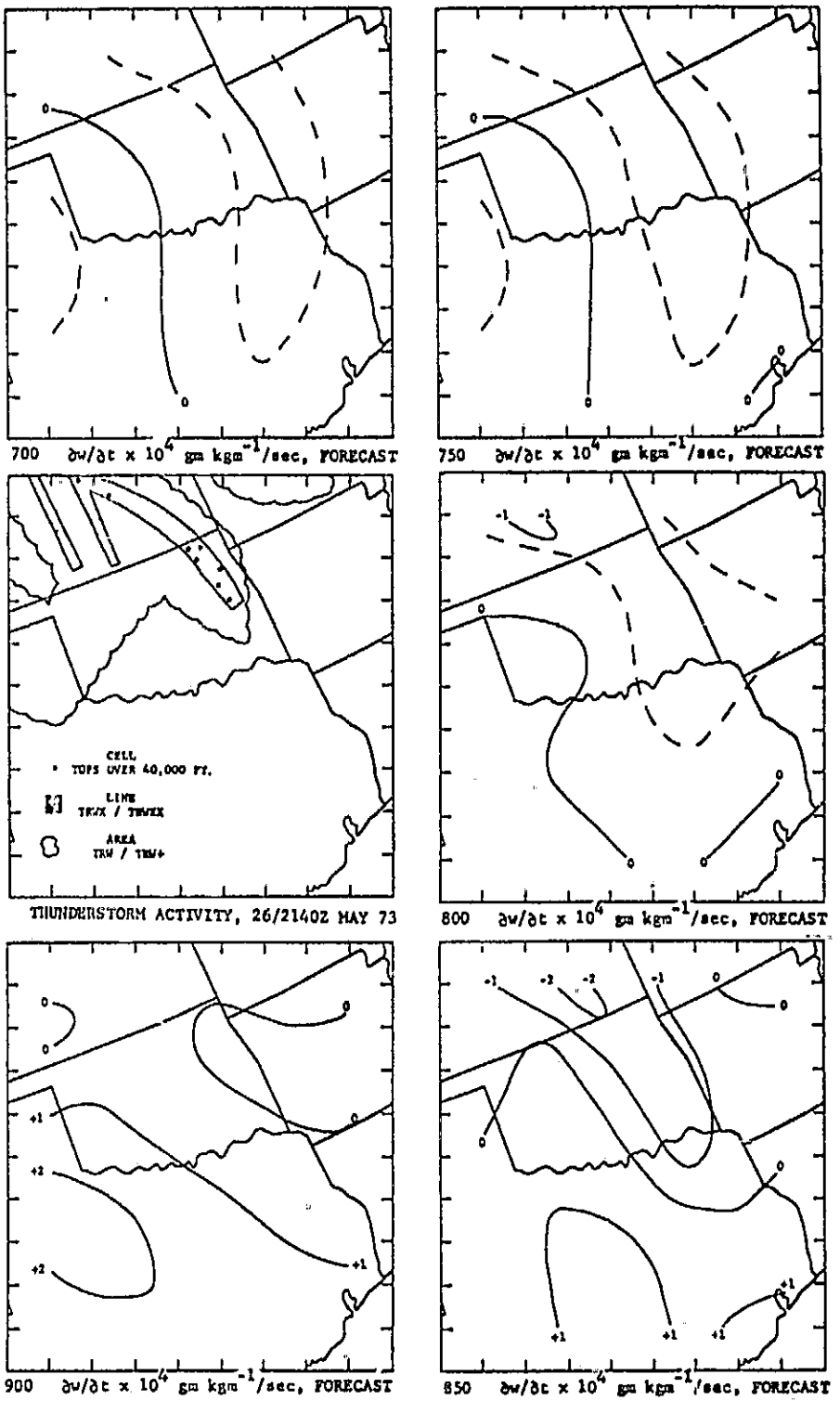

Figure 17. The local change of mixing ratio, $\partial w/\partial t$ x 10^4 gm kgm^{-1}/sec, at the advective forecast time 26/1520Z May 1973.

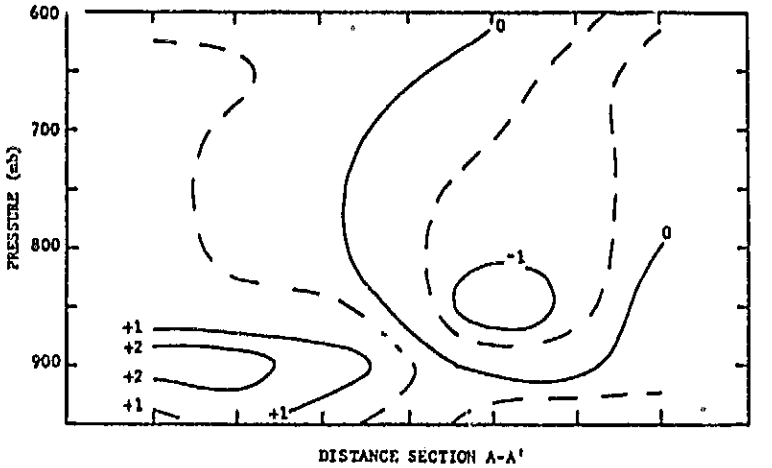

Figure 18. The local change of mixing ratio, $\partial w/\partial t \times 10^4$ gm kgm^{-1}/sec, for the cross-section A-A', at the advective forecast time 26/1520Z May 1973.

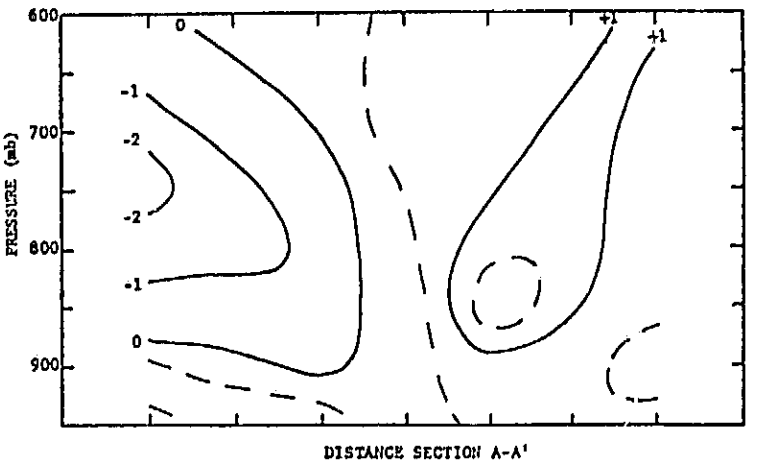

Figure 19. The local change of potential temperature, $\partial\theta/\partial t \times 10^4$ deg K/sec, for the cross-section A-A', at the advective forecast time 26/1520Z May 1973.

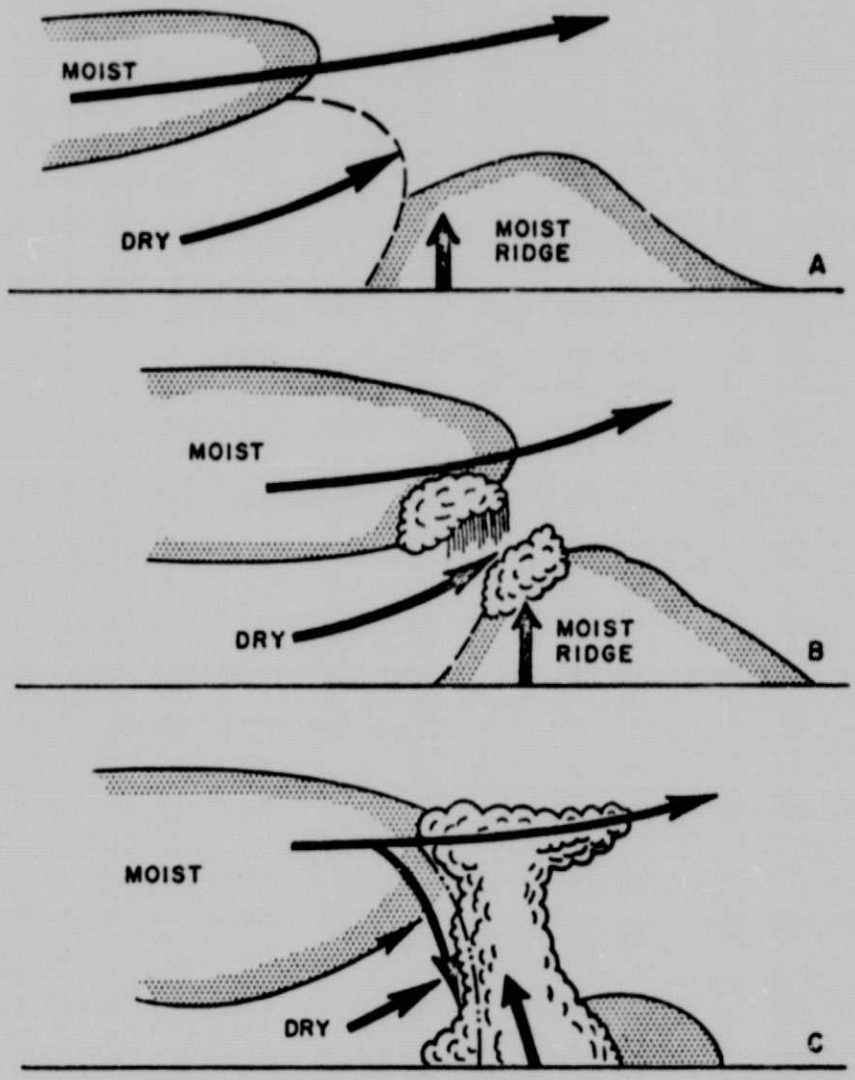

Figure 20. Possible mechanism of squall line development (from Miller, 1972).

CHAPTER VII

SUMMARY AND RECOMMENDATIONS

Several features of the advection analysis with variational optimization analysis techniques are especially noteworthy. The first is inherent with the variational technique; the governing equations and conditions imposed on a model are simultaneously applied. For example, the data filtering is accomplished simultaneously in all dimensions with the ability to specify the amount of scale smoothing for each dimension.

The method of determination of the vertical component of motion is another major feature. The use of the non-homogeneous, anisotropic exponential weight function for the objective analysis of the data fields produces physically realistic divergence values at all pressure levels. These divergence values are then used in a variational technique to determine the vertical motion, within the boundary conditions imposed, consistent with mass continuity. The vertical motion field, crucial to the three spatial dimensional analysis of advection of temperature and mixing ratio, can be assumed to be accurate with a high degree of confidence.

Several promising areas for continued research constitute the final major feature of this research. Research should continue to confirm the existence of the vertical circulation pattern identified with the 26/1200Z May 1973 case study. This vertical circulation may produce

vital clues to the development and maintenance of the severe thunderstorm and its parent squall line.

Another promising area for future research would be the adaptation of the model to a finer mesh grid over a smaller geographical area in order to study the advection fields on the scale of the thunderstorm and its parent squall line. The densely-instrumented Beta network, operated by the National Severe Storms Laboratory, in central Oklahoma is a distinct possibility as the data source. Because the degree of scale smoothing is controllable at each analysis step from the initial objective analysis to the final four dimensional advective analysis, the mesoscale features of interest can be preserved.

The final recommendation for further research is to investigate the short range forecast capabilities of the variational models described. In addition to using the advective patterns and forecast fields to identify the primary areas of squall line initiation several hours in advance, the distinct possibility exists of parameterizing the data to provide severity criteria, such as stability indices. These operational possibilities should be explored in an effort to increase the accuracy of the severe weather watches and warnings.

BIBLIOGRAPHY

Barnes, S. L., 1973: Mesoscale objective map analysis using weighted time-series observations. NOAA Technical Memo ERL NSSL-62, 60 pp.

Blackman, R. B., and J. W. Tukey, 1958: The Measurement of Power Spectra. Dover Press, New York, 190 pp. (Originally published in Bell System Technical Journal, 37).

Davies-Jones, R. P., 1974: Discussion of measurements inside high-speed thunderstorm updrafts. Journal of Applied Meteorology, 13, 710-717.

Gandin, L. S., 1965: Objective Analysis of Meteorological Fields. Israeli Program for Scientific Translations, Jerusalem, 242 pp.

Fankhauser, J. C., 1974: The derivation of consistent fields of wind and geopotential height from mesoscale rawinsonde data. Journal of Applied Meteorology, 13, 637-646.

Foote, G. B., and J. C. Fankhauser, 1973: Airflow and moisture budget beneath a northeast Colorado hailstorm. Journal of Applied Meteorology, 12, 1330-1353.

Haltiner, G. J., 1971: Numerical Weather Prediction. John Wiley & Sons, New York, 317 pp.

Hess, S. L., 1959: Introduction to Theoretical Meteorology. Henry Holt Company, New York, 362 pp.

Hildebrand, F. B., 1965: Methods of Applied Mathematics. Prentice-Hall Inc., Englewood-Cliffs, N.J., 362 pp.

Holton, J. R., 1972: An Introduction to Dynamic Meteorology. Academic Press, New York, 319 pp.

Hylton, D. A., 1972: The application of low-pass and band-pass filtering techniques to surface and upper air fields. Master's Thesis, University of Oklahoma, 79 pp.

Inman, R. L., 1970: Papers on operational objective analysis schemes at the National Severe Storms Forecast Center. NOAA Technical Memo ERL TM-NSSL 51, 91 pp.

Jenkins, G. M., and D. G. Watts, 1968: Spectral Analysis and Its Applications. Holden-Day, San Francisco, 525 pp.

Ketter, R. C., and S. P. Prawel, Jr., 1969: Modern Methods of Engineering Computation. McGraw-Hill, New York, 492 pp.

Lewis, J. M., 1971: Variational Subsynoptic Analysis with Applications to Severe Local Storms. Monthly Weather Review, 99, 786-795.

_____, and T. H. Grayson, 1972: The adjustment of surface wind and pressure by Sasaki's variational matching technique. Journal of Applied Meteorology, 11, 586-597.

Marwitz, J. D., 1972a: The structure and motion of severe hailstorms, Part I: Supercell storms. Journal of Applied Meteorology, 11, 166-179.

_____, 1972b: The structure and motion of severe hailstorms, Part III: Severely sheared storms. Journal of Applied Meteorology, 11, 189-201.

McGinley, J. A., 1973: Environmental energy fields associated with severe storms. Master's Thesis, University of Oklahoma, 129 pp.

Magata, M., and K. Nishida, 1971: On the computational errors in the numerical experiment. Journal of the Meteorological Society of Japan, 49, 774-783.

Miller, R. C., 1972: Notes on analysis and severe-storm forecast procedures of the Air Force Global Weather Central. AWS Technical Report 200 (Rev).

Morris, R. M., 1972: The trowal, an important feature of frontal analysis. Meteorological Magazine, 101, 150-153.

O'Brien, J. J., 1970: Alternative solutions to the classical vertical velocity problem. Journal of Applied Meteorology, 9, 197-203.

Palmen, E., 1967: Evaluation of Atmospheric Moisture Transport for Hydrological Purposes. WMO/IHD Report 1, Geneva, 63 pp.

Pfeffer, R. L., 1962: Results of recent research in meteorology at the Lamont Geological Observatory. Proceedings of the International Symposium on Numerical Weather Prediction in Tokyo. Meteorological Society of Japan, November 7-13, 1960, 249-263.

Sasaki, Y. K., 1969: Proposed inclusion of time variation terms, observational and theoretical, in numerical variational objective analysis. Journal of the Meteorological Society of Japan, 47, 115-124.

_____, 1970a: Some basic formalisms in numerical variational analysis. Monthly Weather Review, 98, 875-883.

_____, 1970b: Numerical variational analysis formulated under the constraints as determined by longwave equations and a low-pass filter. Monthly Weather Review, 98, 884-989.

_____, 1971a: A theoretical interpretation of anisotropically weighted smoothing on the basis of numerical variational analysis. Monthly Weather Review, 99, 698-708.

_____, 1971b: Low-pass and band-pass filters in numerical variational optimization. Journal of the Meteorological Society of Japan, 49, 766-773.

_____, 1973: Mechanism of squall-line formation as suggested from variational analysis of hourly surface observations. Preprints Eighth Conference on Severe Local Storms, Oct. 15-17, American Meteorological Society, Boston, Mass., 8 pp.

_____, and J. M. Lewis, 1970: Numerical variational objective analysis of the planetary boundary layer in conjunction with squall line formation. Journal of the Meteorological Society of Japan, 48, 381-398.

Saucier, W. J., 1955: Principles of Meteorological Analysis. University of Chicago Press, Chicago, 438 pp.

Schaefer, J. T., 1974: The life cycle of the dryline. Journal of Applied Meteorology, 13, 444-449.

Sheets, R. C., 1973: Analysis of STORMFURY data using the variational optimization approach. NOAA Technical Report ERL 265-WMPO 1, 92 pp.

Tegtmeier, S. A., 1974: The role of the surface, sub-synoptic low pressure system in severe weather forecasting. Master's Thesis, University of Oklahoma, 66 pp.

Wagner, K. K., 1971: Variational analysis using observational and low-pass filtering constraints. Master's Thesis, University of Oklahoma, 39 pp.

APPENDIX A

COMPARISON OF CRESSMAN AND ANISOTROPIC EXPONENTIAL WEIGHTING FUNCTIONS—A CASE STUDY

Both the Cressman Weight function and the anisotropic weighting function assign values to grid points from irregularly spaced observation points by using the equation

$$\Phi_{ij} = \frac{\Sigma W_k \Phi_k}{\Sigma W_k}$$

where Φ_k and Φ_{ij} are the variable values at the observation point and grid point respectively and W_k is the weight for that observation point. Each observation is weighted according to a prespecified relationship and the sum of these weighted observations is normalized by the sum of the weights.

Since the Cressman weighting function is distance dependent only, it is isotropic, and because the weighting function is not a function of location, it is also homogeneous. The analysis of a wind field or any other anisotropic, non-homogeneous field with an isotropic, homogeneous weight function is likely to introduce errors into the objective analysis.

In the early stages of this study, the Cressman weighting function was used to objectively analyze the wind fields at each of 19 levels at 50 millibar increments from 1000 to 100 millibars over the 15 by 21 horizontal grid shown in Figure A1. However, at certain levels, the divergence of the horizontal wind was not consistent physically with

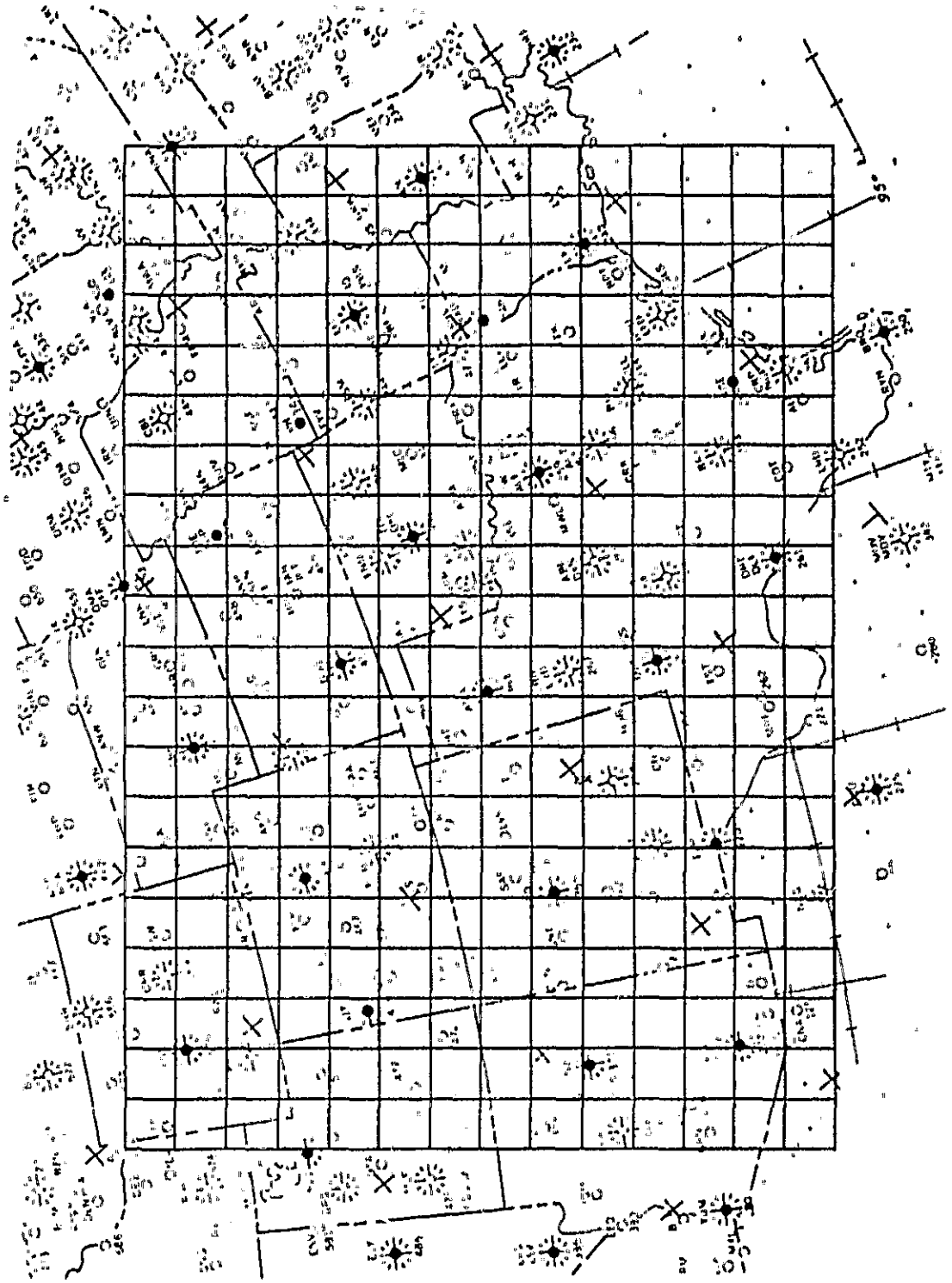

Figure A1. The horizontal grid established for the study. The grid spacing is approximately 125 km. The darkened station circles indicate locations of synoptic upper air reporting stations.

the synoptic situation. Since the accurate computation of the divergence is necessary in this investigation, significant error in the initial objective analysis could easily produce unknown error terms in the remainder of the calculations.

As an example, the divergence field was calculated from the horizontal wind components assigned by a successive correction objective analysis with the Cressman weighting function. The observed data field is shown in Figure A2.

As shown in Figure A2, a closed low height center was in central Texas with a sharp ridge extending from New Mexico through Colorado and Kansas. Wind maxima were present in the northwest and southeast portions of the grid. Synoptically, convergence is associated with the confluence of airflow and divergence is associated with diffluence.

The divergence calculated from the Cressman analysis is shown in Figure A3. The calculated divergence values in northern Arizona and northern New Mexico do not appear to be realistic—apparently the scheme treated the wind at INW (Winslow, AZ) and the wind at ABZ (Albuquerque, NM) to be strongly convergent. Another apparent error exists in northern Texas and central Oklahoma where the very high divergence values appear to be the result of the wind differences at AMA (Amarillo, TX), FTW (Fort Worth, TX), and OKC (Oklahoma City, OK). A streamline analysis suggests significance error.

The same field was then analyzed using an anisotropic exponential weighting function, with only one pass through the data field. The divergence values calculated from these analyses are shown in Figures A4a, A4b, and A4c, and appear much more realistic. Notice that the

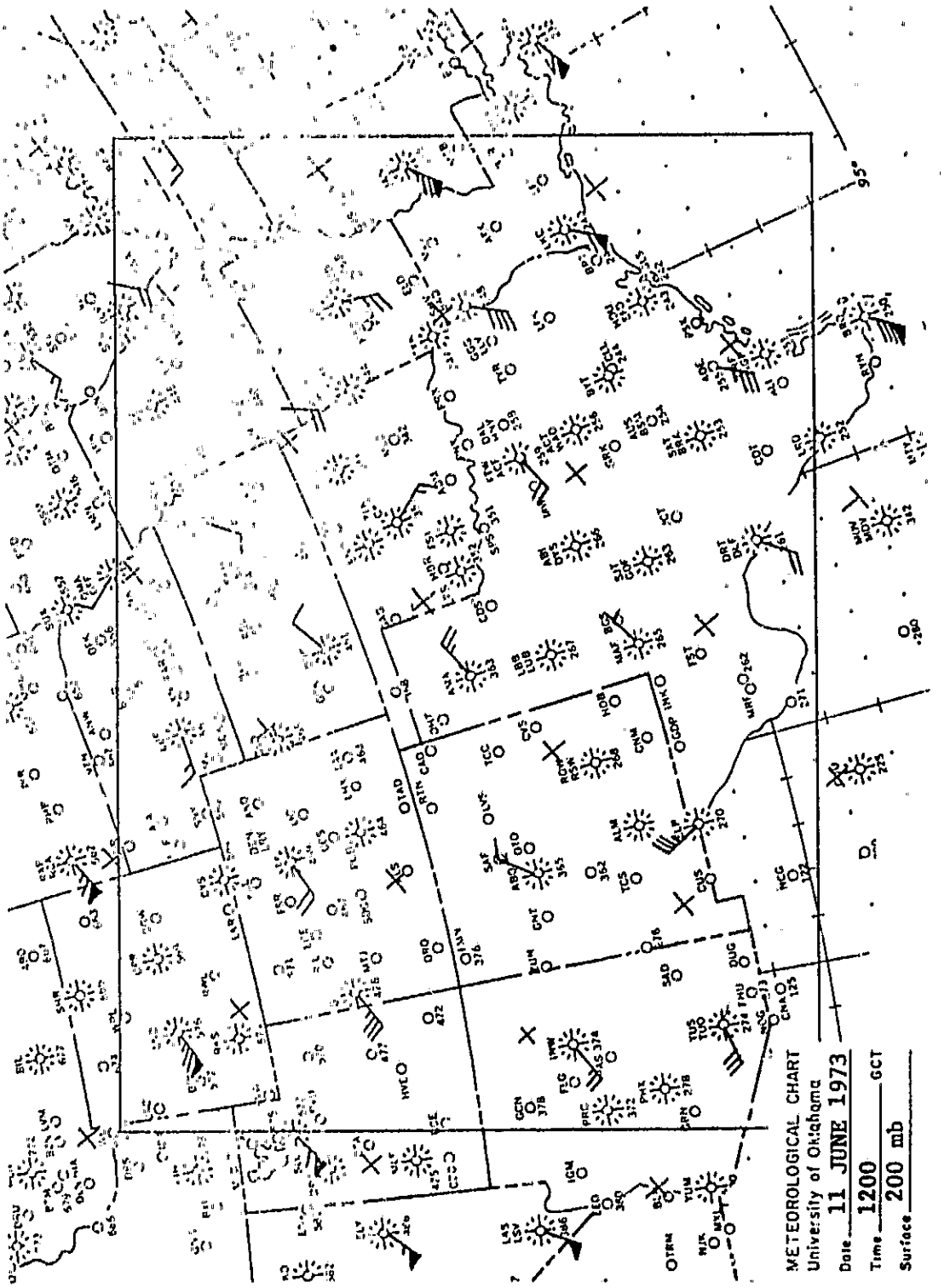

Figure A2. Observed wind field (knots) at 200 mb, 11/1200Z June 1973. The wind field indicates wind maxima in the upper left and lower right portions of the grid, a closed low height center in the lower center and an inclined ridge from the lower left to the upper center.

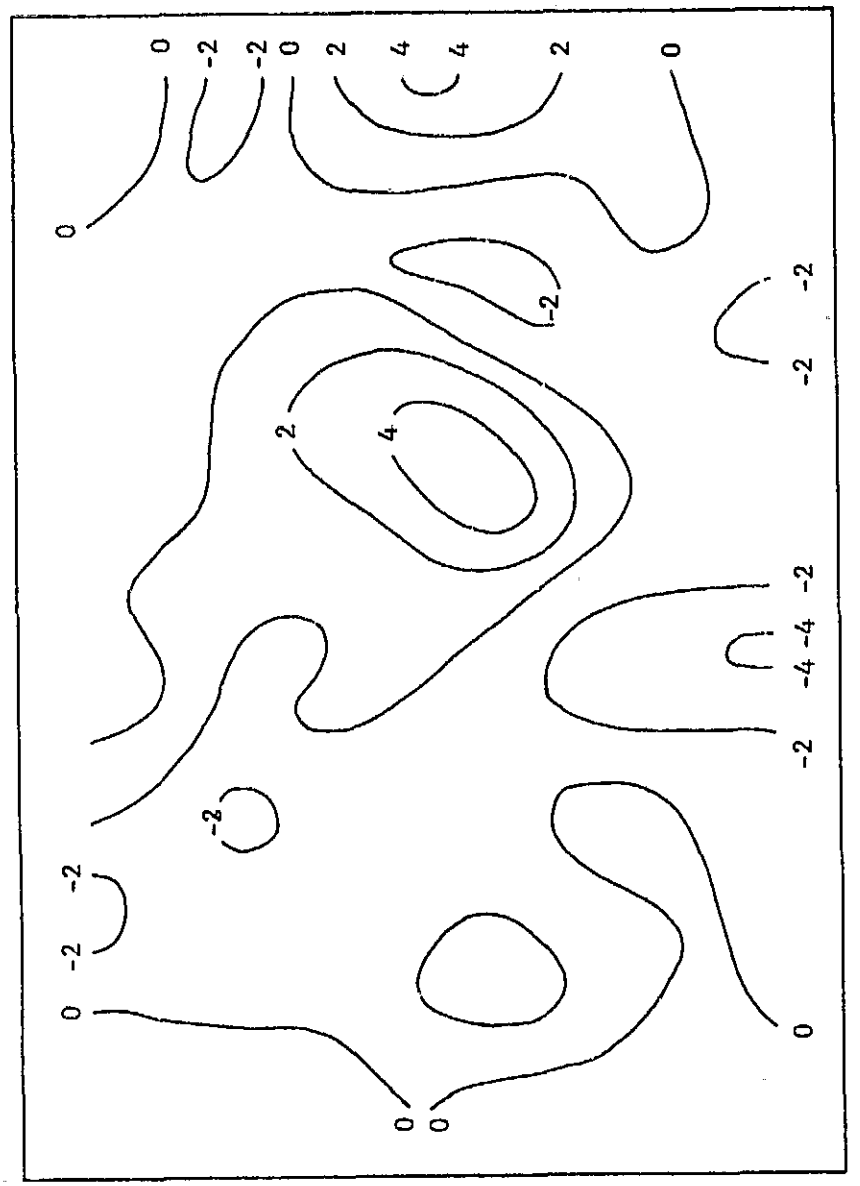

Figure A3. Divergence ($sec^{-1} \times 10^5$) computed from wind field analyzed from Cressman successive correction analysis, 200 mb, 11/1200Z June 1973.

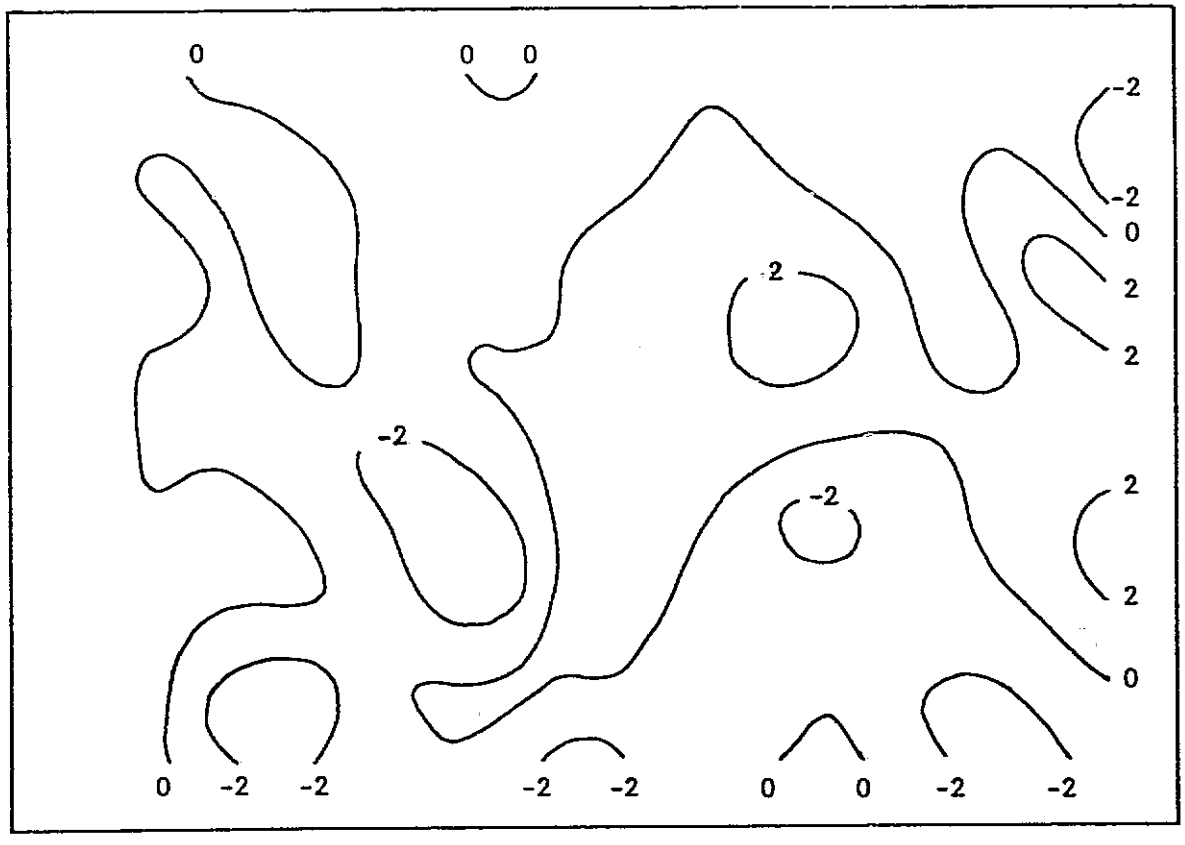

Figure A4a. Divergence ($sec^{-1} \times 10^{5}$) computed from wind field analyzed with anisotropic exponential weight function analysis, 200 mb, 11/1200Z June 1973. For the weight function, $K = 0.5$ and $\beta = 4.0$; the values used in the advection analysis investigations.

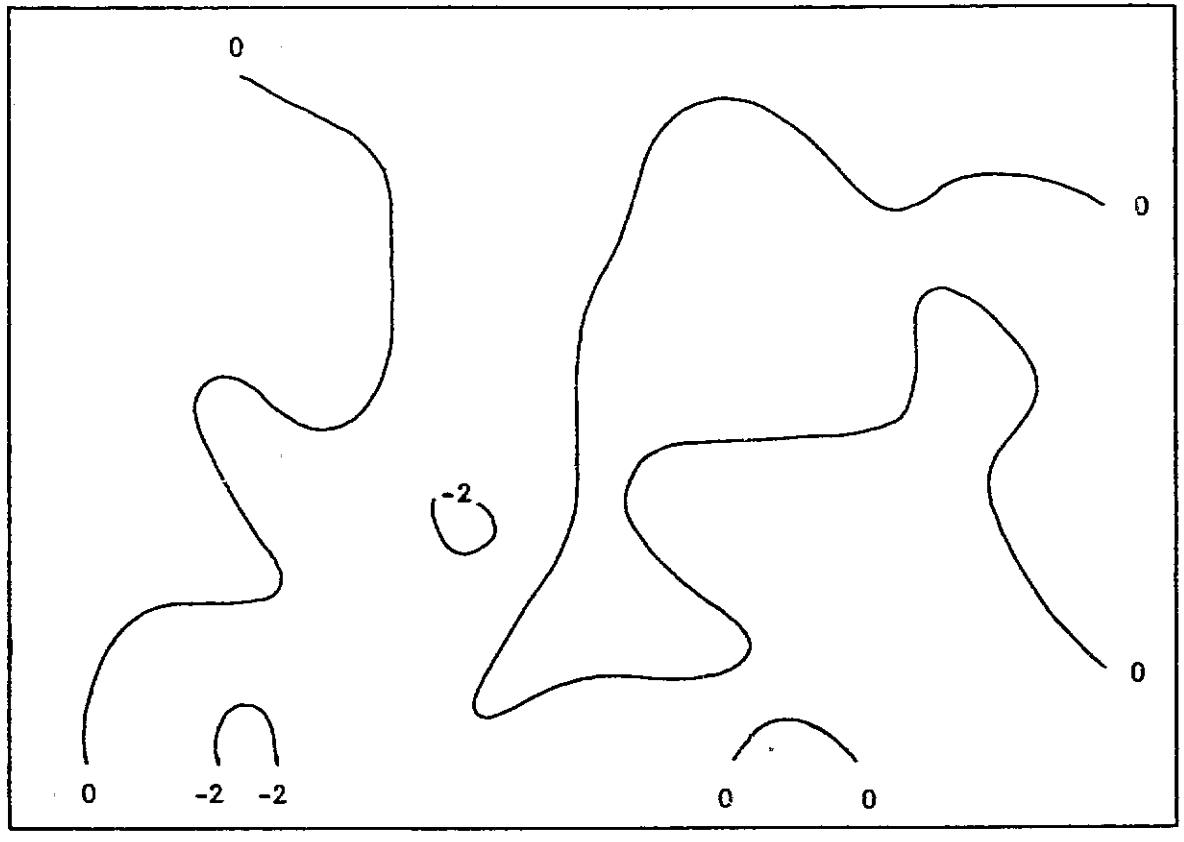

Figure A4b. Divergence ($sec^{-1} \times 10^5$) computed from wind field analyzed with anisotropic exponential weight function analysis, 200 mb, 11/1200Z June 1973 ($K = 1.0$, $\beta = 4.0$).

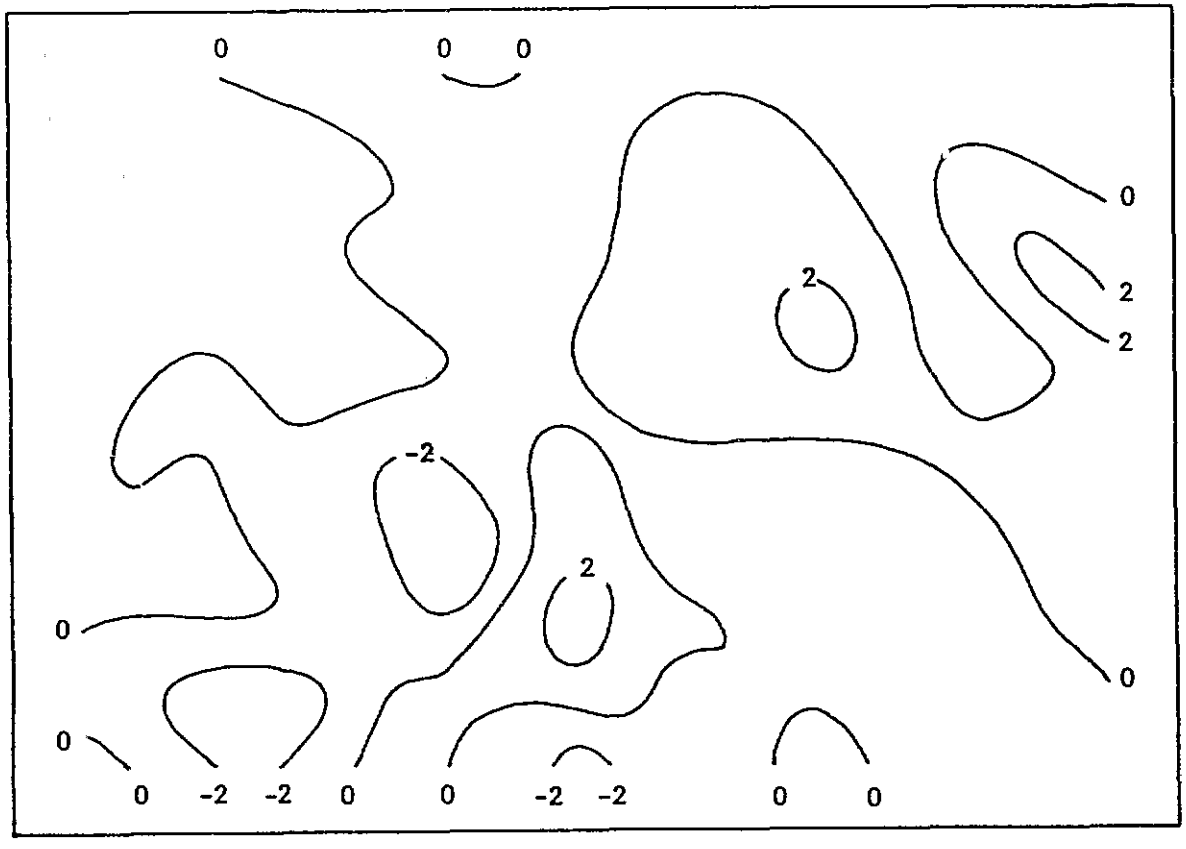

Figure A4c. Divergence ($sec^{-1} \times 10^5$) computed from wind field analyzed with anisotropic exponential weight function analysis, 200 mb, 11/1200Z June 1973 (K = 0.5, β = 9.0).

selection of different sets of K and β change the magnitudes but not the patterns of divergence.

The divergence values calculated from the Cressman analysis have a greater magnitude, even though the patterns were derived from wind fields subjected to greater implicit smoothing than in the analysis based on the new weighting function. Also, a comparison of the divergence patterns shows significant differences in sign of the divergence as well as the magnitude. The differences are most pronounced in the vicinity of the smaller wavelength features of primary interest to the advection investigations.

The differences appear to be a function of the isotropy of the Cressman weight function; perhaps any isotropic weighting function will introduce significant error, which would affect the validity of the computations and conclusions of later parts of the study. In any event, the necessity of accuracy in the initial objective analysis of the data field is emphasized.

APPENDIX B

THE USE OF VARIATIONAL OPTIMIZATION ANALYSIS IN DATA FILTERING

Variational calculus may be used to find the stationary points of a functional, an integral of a function which may be composed of several dependent variables and their first and second order time and space derivatives, in a manner analogous to the use of differential calculus to find the stationary points of a function with regard to each of its variables. When the functional is in quadratic form, the stationary values of the functional will be minimum (Sasaki, 1970a).

The functional is composed of a series of weighted terms representing conditions to be satisfied, either exactly with strong constraint weighting or approximately with weak constraint weighting. The strong constraint weights are termed Lagrange multipliers and are treated as introduced dependent variables with respect to the functional. The terms representing conditions to be exactly satisfied are premultiplied by a Lagrange multiplier for inclusion in the functional (Sasaki, 1970a). For terms representing conditions to be approximately satisfied, the square of the term is multiplied by a variable independent of the functional. This term is known as a weak constraint; terms with a Lagrange multiplier are known as strong constraints. These weak and strong constraints may represent the model dynamics, kinematics, thermodynamics, and energetics. One weak constraint term common to the majority of all functionals is the observational constraint, a weak

constraint, which relates the observed or initial field (the "tilde" field) to the true field, or that which satisfies all constraints in the formalism. By specifying the observational constraint weight, the amount of departure from the initial field can be controlled.

This ability of the variational optimization analysis method to simultaneously impose dynamic, statistical, kinematic, and other conditions in both diagnostic and prognostic forms is perhaps the major advantage of the variational method (Sasaki, 1971). The most important uses of variational optimization analysis have been in data filtering and in the initial assignment of data fields consistent with the dynamics or other conditions of the model incorporating the data. Thus, a geostrophic forecast model can be initialized with wind and geopotential height fields adjusted to geostrophic balance.

Each term or squared expression in the functional is minimized; as many terms as can be adequately treated analytically and computationally may be added to the functional. However, due to noise and unresolvable wavelengths in the data, not all conditions can be simultaneously exactly satisfied. The degree to which a condition must be satisfied can be specified through the assignment of the weights to the weak constraints. A low value of a weight will allow more deviation from the constraint than a high value.

The weak constraint weights are specified independent of the functional but may vary as a function of the spatial and temporal coordinates. The value of the weights may be determined empirically from examination of the final or true data fields, from statistical descriptions of the data fields, from <u>a priori</u> knowledge of the reliability

or accuracy of the data, which may be a function of source, time, location, or observation method; and from analytic solutions of the analysis equations derived from the variational formalism. For the simpler finite difference approximations and assumed wave forms of the solution data fields, the response function for varying weights can be determined.

In a low pass filter, the desired result is to suppress the amplitudes in the higher frequencies in the data field by locally altering the values of the data. This can be accomplished with variational optimization analysis by including first derivative terms as weak constraints in the functional (second derivative terms, representing curvature, may also be used (Wagner, 1971)). A high frequency in the observed data field would appear as locally large slope values; the effect of the weak constraint as the first derivative is to strongly reduce locally large slope values and to have little effect on the low slope values representing low frequencies in the data.

The variational functional selected as the filter contains an observational constraint and the first derivative constraints in three dimensions. The functional is

$$J = \iiint \Big\{ \tilde{\alpha}\left[(u-\tilde{u})^2 + (v-\tilde{v})^2\right] + \alpha_f\left[\left(\frac{\partial u}{\partial x}\right)^2 + \left(\frac{\partial u}{\partial y}\right)^2 + \left(\frac{\partial v}{\partial x}\right)^2 + \left(\frac{\partial v}{\partial y}\right)^2\right] + \alpha_p\left[\left(\frac{\partial u}{\partial p}\right)^2 + \left(\frac{\partial v}{\partial p}\right)^2\right]\Big\} dp\ dy\ dx \qquad (1)$$

where $\tilde{\alpha}$, α_f and α_p are the weak constraint weights; u and v are the analyzed fields and $\tilde{u}$ and $\tilde{v}$ are the observed or assigned fields.

The stationary value of the functional is found by equating the first variation of the functional to zero. Some basic properties

of the variational operator, δ, are:

1. Variation and differentiation are permutable (Sasaki and Lewis, 1970; Sheets, 1973).

2. Variation and integration are permutable (Sasaki and Lewis, 1970; Sheets, 1973).

3. In finite difference form summed over the domain, the commutation property of the variation is (from Sasaki, 1969; Wagner, 1971):

$$\Sigma\Phi\nabla\delta\Psi = -\Sigma\delta\Psi\nabla\Phi$$

4. In the following derivations, each variable ϕ varies by an arbitrary non-zero amount $\delta\Phi$ in the interior. $\delta\Phi$ is zero on the boundaries as the boundary condition.

5. The variational operator acts on all variables in much the same way as a partial differential operator. The laws of variation of sums, products, ratios, and powers are completely analogous to the corresponding laws of differentiation (Hildebrand, 1965).

The derivation of the Euler-Lagrange equation in the finite difference form for numerical solution is, where X, Y, and P are the summation domains:

$$\delta J = 0 = \sum_X \sum_Y \sum_P \delta[\tilde{\alpha}\{(u-\tilde{u})^2 + (v-\tilde{v})^2\} + \alpha_f\{(\nabla_x u)^2 + (\nabla_y u)^2 + (\nabla_x v)^2 + (\nabla_y v)^2\} + \alpha_p\{(\nabla_p u)^2 + (\nabla_p v)^2\}] \quad (2)$$

$$\delta J = 0 = \sum_X \sum_Y \sum_P 2\tilde{\alpha}(u-\tilde{u})\delta u + 2\tilde{\alpha}(v-\tilde{v})\delta v + \alpha_f\{2\nabla_x u\nabla_x \delta u + 2\nabla_y u\nabla_y \delta u\} + \alpha_f\{2\nabla_x v\nabla_x \delta v + 2\nabla_y v\nabla_y \delta v\} + \alpha_p\{2\nabla_p u\nabla_p \delta u + 2\nabla_p v\nabla_p \delta v\} \quad (3)$$

Use of the commutation properties of the variational operator produces

$$\delta J = 0 = \sum_X \sum_Y \sum_P [\tilde{\alpha}(u-\tilde{u}) - \alpha_f\nabla_x^2 u - \alpha_f\nabla_y^2 u - \alpha_p\nabla_p^2 u]\, 2\delta u + [\tilde{\alpha}(v-\tilde{v}) - \alpha_f\nabla_x^2 v - \alpha_f\nabla_y^2 v - \alpha_p\nabla_p^2 v]\, 2\delta v \quad (4)$$

Since the variation is arbitrary on the interior, the only way that δJ can be zero is for the coefficients of δu and δv to be zero. This condition forms the Euler-Lagrange equations

$$\alpha_f (\nabla_x^2 u + \nabla_y^2 u) + \alpha_p \nabla_p^2 u - \tilde{\alpha} u = - \tilde{\alpha}\tilde{u} \qquad (5)$$

$$\alpha_f (\nabla_x^2 v + \nabla_y^2 v) + \alpha_p \nabla_p^2 v - \tilde{\alpha} v = - \tilde{\alpha}\tilde{v} \qquad (6)$$

These decoupled equations form the analysis equations. They are elliptic partial differential equations which can be solved by Richardson or Liebmann relaxation numerical techniques.

The relaxation technique for specified boundary values is a convergent, iterative process in the grid interior. The initial fields form the first guess field, a residual is computed and a correction is applied to the current value, and the iteration continues until there is convergence to a pre-selected tolerance. In the use of the variational technique to filter data fields, the author noted that convergence was significantly increased by eliminating sharp gradients on the boundaries with a Hanning filter (Blackman and Tukey, 1958). The boundaries then remain constant during the relaxation.

To solve the analysis equations, equations (5) and (6) are expressed in center-space finite difference form and then non-dimensionalized and scaled so that the terms are of the same magnitude in the analysis equations. The center space finite difference form for a three-dimensional grid with the i, j, and k directions correspond to x,y, and p respectively. Equation (5) becomes

$$\frac{\alpha_f}{d^2} (u_{i,j+1,k} + u_{i,j-1,k} + u_{i+1,j,k} + u_{i-1,j,k} - 4u_{i,j,k} +$$

$$\frac{\alpha_p}{h^2} (u_{i,j,k+1} + u_{i,j,k-1} - 2u_{i,j,k}) - \tilde{\alpha} u_{i,j,k} + \tilde{\alpha}\tilde{u}_{i,j,k} = 0 \qquad (7)$$

where d is the grid distance in the i and j directions and h is the grid distance in the k direction.

Collect terms and rewrite as

$$\frac{\alpha_f}{d^2}\left(u_{i,j+1,k} + u_{i,j-1,k} + u_{i+1,j,k} + u_{i-1,j,k}\right) + \frac{\alpha_p}{h^2}\left(u_{i,j,k+1} - u_{i,j,k+1}\right) = A$$

$$\left(-\tilde{\alpha} - \frac{4\alpha_f}{d^2} - \frac{2\alpha_p}{h^2}\right) u_{i,j,k} = B\, u_{i,j,k} \tag{8}$$

$$\tilde{\alpha}\,\tilde{u}_{i,j,k} = C$$

thus, $B\, u_{i,j,k} + A + C = 0$ is the desired numerical solution. For the n^{th} iterative pass (and notationally dropping the subscripts of u),

$$B\, u^n + A^n + C = \text{Residual}^n \tag{9}$$

when a correction is applied to u, the residual vanishes to produce

$$B\, u^{n+1} + A^n + C = 0 \tag{10}$$

If equation (10) is subtracted from (9), the result is

$$u^{n+1} = u^n - \frac{\text{Residual}^n}{B} \tag{11}$$

Substitution of B back into the expression produces

$$u^{n+1} = u^n + \frac{\text{Residual}^n}{\tilde{\alpha} + \frac{4\alpha_f}{d^2} + \frac{2\alpha_p}{h^2}} \tag{12}$$

The substitution of (9) into (12) produces the correction to apply u sequentially at each grid point until the desired convergence is achieved. This is

$$u^{n+1} = u^n + \frac{A^n + Bu^n + C}{\tilde{\alpha} + \frac{4\alpha_f}{d^2} + \frac{2\alpha_p}{h^2}} \tag{13}$$

or $$(\tilde{\alpha} + \frac{4\alpha_f}{d^2} + \frac{2\alpha_p}{h^2})u^{n+1}_{i,j,k} = \tilde{\alpha}\tilde{u}_{i,j,k} + \frac{\alpha_p}{h^2}(u^n_{i,j,k} + u^n_{i,j,k-1}) + \frac{\alpha_f}{d^2}(u^n_{i,j+1,k} + u^n_{i,j-1,k} + u^n_{i+1,j,k} + u^n_{i-1,j,k}) \quad (14a)$$

and $$(\tilde{\alpha} + \frac{4\alpha_f}{d^2} + \frac{2\alpha_p}{h^2})v^{n+1}_{i,j,k} = \tilde{\alpha}\tilde{v}_{i,j,k} + \frac{\alpha_p}{h^2}(v^n_{i,j,k+1} + v^n_{i,j,k-1}) + \frac{\alpha_f}{d^2}(v^n_{i,j+1,k} + v^n_{i,j-1,k} + v^n_{i+1,j,k} + v^n_{i-1,j,k}) \quad (14b)$$

To examine the analytical response function, which is defined as the ratio of the analyzed wave amplitude to the initial wave amplitude as a function of wavelength, assume that u and $\tilde{u}$ have the analytic form

$$\tilde{u} = \tilde{A}\, e^{i(kx + ky + np)} \quad (15)$$

$$u = A\, e^{i(kx + ky + np)} \quad (16)$$

where k and n are wave numbers in the horizontal and vertical directions, and substitute into the analysis equations (5) and (6). For the analysis equation for u only, after the substitution of (15) and (16) into (5), carrying out the indicated differentiation (in continuous form), and canceling the exponential term which remains unchanged, the result is

$$-2k^2\alpha_f A - n^2\alpha_p A = \tilde{\alpha}(A-\tilde{A}) \quad (17)$$

Expressing the analytic response function, R, as $A/\tilde{A}$, the response function is

$$R = (1 + \frac{2k^2\alpha_f}{\tilde{\alpha}} + \frac{n^2\alpha_p}{\tilde{\alpha}})^{-1} \quad (18)$$

To determine the filter response function of the finite difference analog, we need initially consider only the response in the x

direction. The assumed forms of the analyzed and initialized u fields are, in finite difference form

$$u = A\, e^{i(kr\Delta x)} \tag{19a}$$

$$\tilde{u} = \tilde{A}\, e^{i(kr\Delta x)} \tag{19b}$$

where $k = 2\pi/L$, the wave number, and $x = r\Delta x$, and Δx = grid spacing. The analysis equation (7) in the x direction is

$$\frac{\alpha_f}{\Delta x^2}\left[u_{i+1} + u_{i-1} - 2u_i\right) = \tilde{\alpha}(u-\tilde{u}) \tag{20}$$

Substitution of equations (19a) and (19b) into (20) produces

$$\frac{A\alpha_f}{\Delta x^2}\left[\exp(ik(n+1)\Delta x) + \exp(ik(r-1)\Delta x) - 2\exp(ikr\Delta x)\right]$$

$$= \tilde{\alpha}(A-\tilde{A})\exp(ikr\Delta x) \tag{21}$$

Cancellation of the exponential term yields

$$\frac{A\alpha_f}{\Delta x^2}\left(e^{ik\Delta x} + e^{-ik\Delta x} - 2\right) = \tilde{\alpha}(A-\tilde{A}) \tag{22}$$

Use of the identities

$$2\cos(x) = e^{ix} + e^{-ix}$$

$$2\cos(2x) - 2 = -4\sin^2(x)$$

produces

$$\frac{\alpha_f}{\Delta x^2}\left(-4\sin^2(k\Delta x/2)\right) = \frac{\tilde{\alpha}}{A}(A-\tilde{A}) \tag{23}$$

which simplifies to the response function

$$R_x = \frac{\tilde{A}}{A} = \left(1 + \frac{4\alpha_f}{\tilde{\alpha}\Delta x^2}\sin^2\left(\frac{\pi}{L}\Delta x\right)\right)^{-1} \tag{24}$$

Similarly, the response function in the p plane is

$$R_p = \left(1 + \frac{4\alpha_f}{\alpha \Delta p^2} \sin^2 \left(\frac{\pi}{p} \Delta p\right)\right)^{-1} \qquad (25)$$

The low pass filter characteristics of the first derivative filter may easily be verified from equation (24). As the wavelength L, expressed as a multiple of Δx, increases from twice the grid spacing (which corresponds to the Nyquist frequency) to large values, the filter response function approaches a value of 1; i.e., no amplitude change for that wavelength. As with the majority of filtering techniques, aliasing will occur for frequencies greater than the Nyquist frequency, the highest resolvable frequency. Since the Nyquist frequency is defined in terms of the grid spacing, the filtering characteristics are a function of the grid spacing. It is advantageous therefore to select a grid interval smaller than the data measurement point spacing. This results in a greater discriminatory filtering capability.

To this point, the equations and derivations may be regarded as either dimensional or as scaled and dimensionless. However, the computations and the selection of the weights are simplified when the equations are in scaled, non-dimensional form.

For the analysis equation (5)

$$\alpha_f \left(\nabla_x^2 u + \nabla_y^2 u\right) + \alpha_p \left(\nabla_p^2 u\right) - \tilde{\alpha}\, u = - \tilde{\alpha}\, \tilde{u}$$

let each variable be the product of a "star" term and a "prime" term where the primed term is dimensionless and of the magnitude of one.

Thus,

$$\alpha_f = \alpha_f^* \alpha_f'$$

$$\alpha_p = \alpha_p^* \alpha_p'$$

$$\tilde{\alpha} = \tilde{\alpha}^* \tilde{\alpha}'$$

$$u = u^* u'$$

$$\tilde{u} = u^* \tilde{u}'$$

and,

$$\nabla_x^2 = \frac{1}{d^2} \nabla_x^{2'}$$

$$\nabla_y^2 = \frac{1}{d^2} \nabla_y^{2'}$$

$$\nabla_p^2 = \frac{1}{h^2} \nabla_p^{2'}$$

The substitution of the variables and operators into equation (5) and the collection of all dimensional terms produces

$$\left(\frac{\alpha_f^*}{\tilde{\alpha}^* d^2}\right) \alpha_f' \left(\nabla_x^{2'} u' + \nabla_y^{2'} u'\right) + \left(\frac{\alpha_p^*}{\tilde{\alpha}^* h^2}\right) \alpha_p' \nabla_p^{2'} u' = \tilde{\alpha}'(u' - \tilde{u}') \qquad (26)$$

The selection of the scale values is largely independent on the scales of interest in the study and the grid spacing established. For this study, the scale values are

$$u^* = 10 \text{ m/sec}$$

$$d \doteq 125 \text{ km}$$

$$h = 50 \text{ mb}$$

To reduce the left hand side of equation (26) to the order of magnitude of one, select

$$\tilde{\alpha}^* = 1$$

$$\alpha_f^* = d^2$$

$$\alpha_p^* = h^2$$

Equation (26) then becomes identical to the form used in derivation of the filter response. The only difference is that variables and parameters have scaled, non-dimensional values. For example, in equation (24), the dimensional value of Δx^2 is near $(125\ km)^2$; the non-dimensional value of Δx^2 is $(1)^2$.

The response function of equations (24) and (25) may easily be calculated for any wave length in multiples of the grid spacing. The response functions for both first derivative filters and second derivative filters are published by Wagner (1971). The response function for the first derivative filter term comprises a family of curves. Since the measurement point spacing (not the grid spacing) in the horizontal and vertical defines the minimum resolvable wavelengths in the data, the filtering response should differ for horizontal and vertical wavelengths. This is controllable by adjusting the ratio of the non-dimensional weights, as shown in Wagner's study. The response functions shown in Figure B1 illustrate the family of response functions for this investigation.

It should be noted that this filter technique does not produce a phase shift or frequency change. This feature is found in other finite difference filters (Haltiner, 1971).

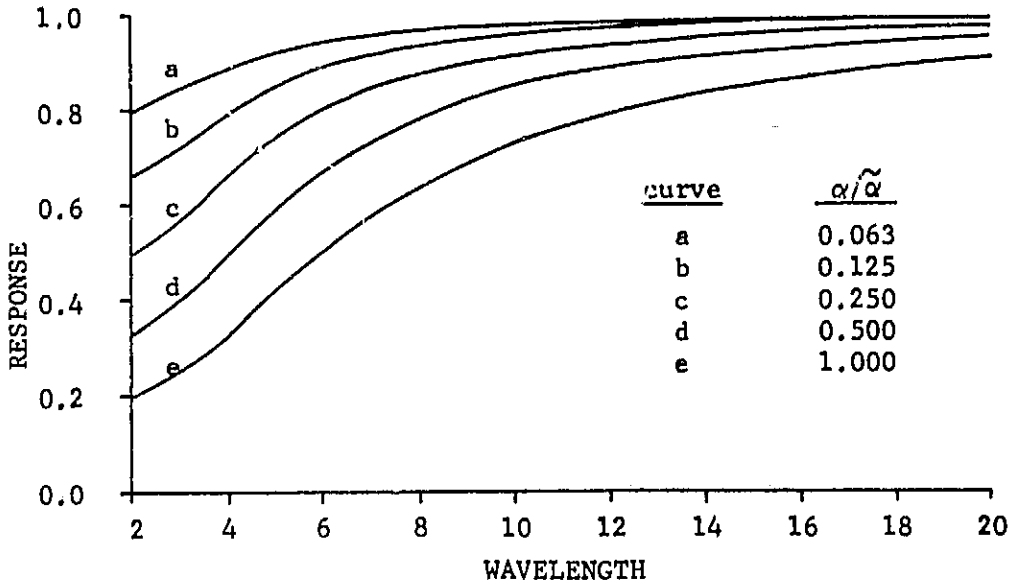

Figure B1. Response function of the first derivative filter as a function of wavelength, expressed as multiples of the grid interval, for varying ratios of filter weight, α, to observational weight, $\tilde{\alpha}$.

APPENDIX C

SEVERE THUNDERSTORM DEVELOPMENT THROUGH THE WARM, DRY INTRUSION

The initial conditions at 26/1200Z May 1973 and the advective forecasts from the variational model indicated that at the time and location of squall line development, the low-level moist air was overlain by a deep layer of warm, very dry air. The presence of the thunderstorms thus indicates an indirect circulation; cooler moist air is rising convectively through the warmer, dry layer above. At cloud base, the thunderstorm updraft air would be negatively buoyant with respect to the mesoscale environmental conditions. The existence of this indirect circulation is supported by an examination of the ATS III imagery for 26/1200Z May 1973 in conjunction with the variational model results. Six selected frames with brief descriptions are included as Figures C1 to C6.

Figure C1 depicts the pre-thunderstorm environment. The warm, dry air of the dry intrusion extends eastward over the stratus in eastern Oklahoma (apparent also in Figure 3, the Tinker AFB sounding) from the surface position to the west of the stratus boundary. The initial thunderstorm development occurred on the western boundary of the moist air. This is a preferred location for squall line thunderstorm development (Tegtmeier, 1974), which agrees well with Schaefer's model of the relation of the surface dryline to the inversion marking the lower boundary of the dry intrusion (Schaefer, 1974).

As the thunderstorms develop, the warm, dry air continues to advect toward the east, as shown in Figures C3 to C5. This eastward advection is indicated also in the forecasts from the variational advective model as depicted in Figures 15 and 19, for example.

The mesoscale environment of the severe thunderstorms shown in Figures C5 and C6 appears to be a low level moist layer (below 850 mb), capped by an air inversion marking the boundary between the moist air and the much warmer dry air intrusion, which extends at least through the 700 mb level. The mesoscale environment thus indicates an indirect convective circulation below the 700 mb level; cool moist air rises convectively through warmer, dry air.

As the thunderstorms develop to severe levels, they significantly modify their mesoscale environment in the vicinity of the storm and in the area downwind from the storm, since the storms typically translate at a rate less than that of the environmental winds. The scale interactions which exist at the levels of the dry air intrusion immediately upwind of the storm may be a significant factor in the development of the storm to severe levels. The variational advective forecast results indicate that the intrusion is very dry, with virtually an unlimited capacity for evaporation, and warm with a near neutral lapse rate. Thus, evaporation of cloud material into the dry air would produce a strong subsistance of the cooler air, especially since even with a dry adiabatic descent, the equilibrium level may be several hundred millibars below the original level of cooling. As surface heating warms the cooler layer beneath the inversion, this subsiding air may reach the surface.

A major effect of the warm, dry intrusion in the severe storm

environment is to facilitate a detrainment of the storm air into the mesoscale environmental air, as opposed to the entrainment of environmental air into the storm. The zone where rapid evaporative cooling occurs will protect the storm updrafts from the dry environmental air, and perhaps is necessary for development to severe levels.

Recent published research on severe storms support detrainment into the dry intrusion (Davies-Jones, 1974; Marwitz, 1972a and 1972b; Foote and Fankhauser, 1973). Davies-Jones observed that soundings in severe storm updrafts indicated that the cores of strong updrafts were undiluted by the environmental air. He also observed that the sounding balloons rose almost vertically in the storm in spite of pronounced environmental shear. A negative buoyancy at cloud base was observed from aircraft measurements by Marwitz. Based on time-section analyses of two storms, Marwitz inferred that the descending air to the southwest (the windward side) of the thunderstorms had subsided from above the cloud base. He suggested that this mid-tropospheric air is directed downward as a result of evaporative cooling and deflection; this subsiding air reaching the surface layers could intensify the gust front.

Foote and Fankhauser (1973) state that negatively buoyant inflow air is a fairly general observation for large, persistent storms and conclude that dynamic forcing drives the low-level inflow into the storm. Correlations of the surface conditions, as indicative of the low-level inflow, with squall line thunderstorm development have been good. Sasaki (1973) concluded that intense surface moisture convergence coincides to squall line development and local severe weather areas and that a local downward momentum transport is very important to squall line formation.

The role of the dry air intrusion to severe storm development is as yet speculative. The scale interactions are difficult to parameterize, describe, and model and the measurements made of severe thunderstorms may sample either the mesoscale unaltered environmental conditions, the thunderstorm scale conditions, or the interacting zones. Some conclusions may be hypothesized, however. The warm, dry intrusion facilitates detrainment with a resulting downward transport of modified air and deflection of environmental air. This mechanism provides for a protection of the storm interior from the dry air and the environmental shear through the dry layer. The subsiding air provides for a downward momentum transport and will serve to intensify the gust front. Another significant factor not directly commented upon is that the inversion layer marking the lower boundary of the dry intrusion serves to cap the potential instability of the moist air below. The relation of the dry intrusion to the initial development of thunderstorms was not indicated in the variational advective model results.

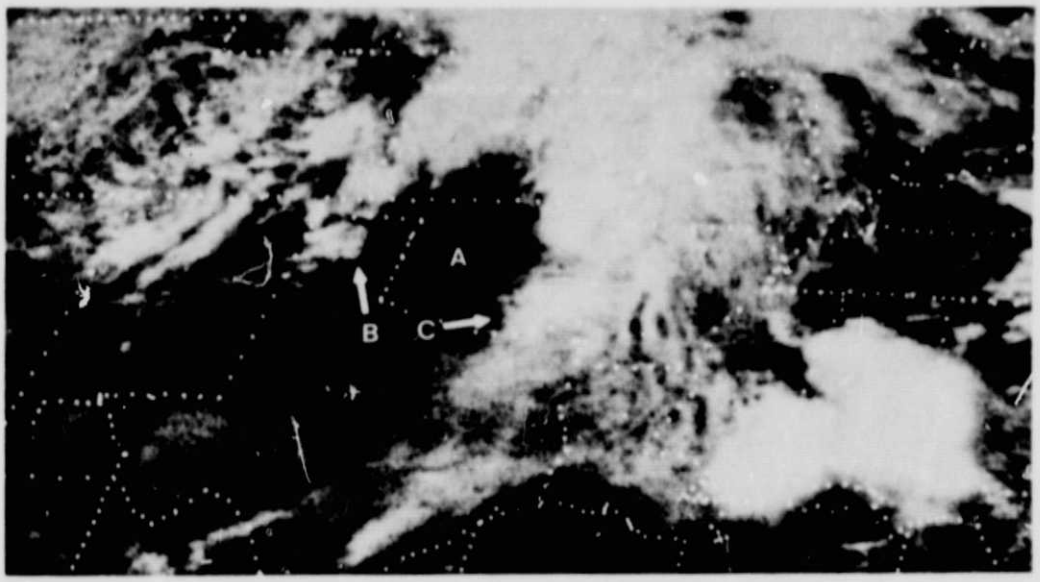

Figure C1. ATS III, 26/1819Z May 1973. The location of the dry air intrusion is approximated by the clear area, indicated by A. The cloudiness B is associated with the southeastward moving cold front from the low pressure center in central Kansas. The cloudiness C is stratiform beneath the dry air intrusion. There is no thunderstorm activity in Oklahoma at this time.

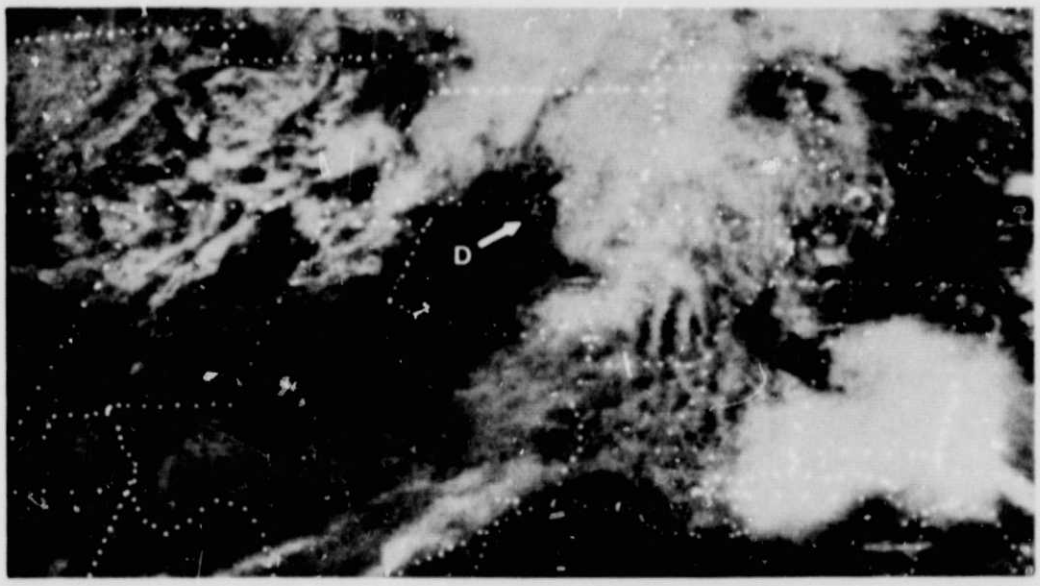

Figure C2. ATS III, 26/1858Z May 1973. The location of the first reported thunderstorms in Oklahoma is indicated by D.

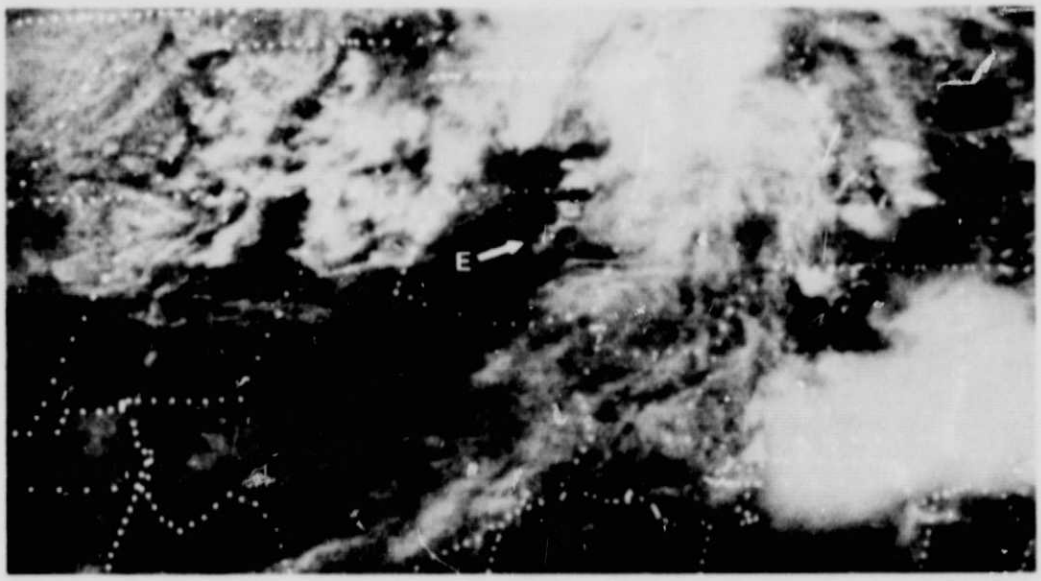

Figure C3. ATS III, 26/2006Z May 1973. The thunderstorm activity in Oklahoma has developed southward and is aligned as the well-defined squall line E.

Figure C4. ATS III, 26/2031Z May 1973. The rapid development of the squall line E in the 25 minutes between Figure C3 and Figure C4 is very apparent. The first of the numerous tornadoes with this squall line was reported at 2052Z with the thunderstorm in Kansas just north of the Oklahoma border. Tornadoes were also reported at 2051Z with the thunderstorm complex G in southern Kansas.

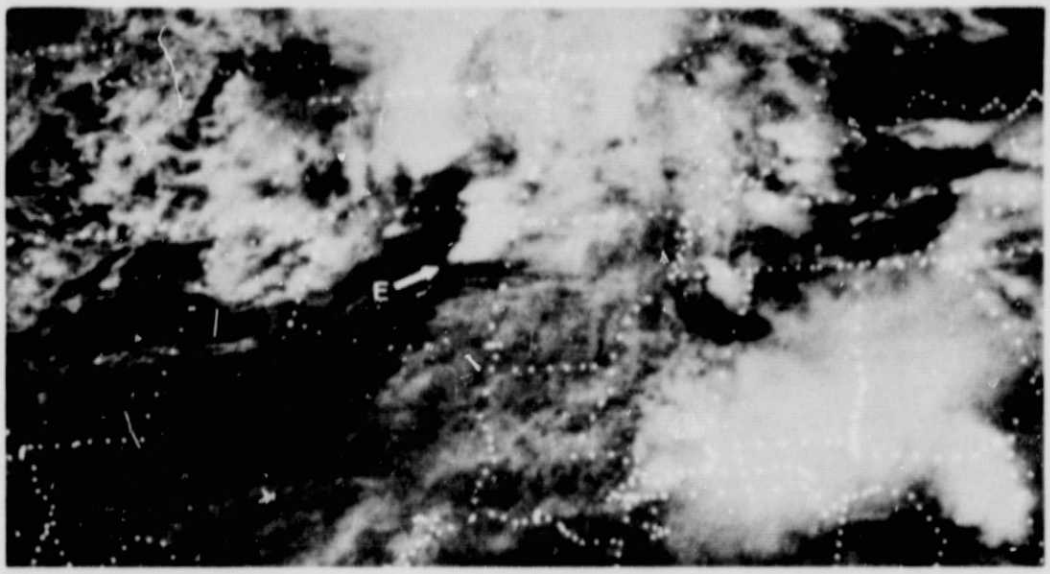

Figure C5. ATS III, 26/2110Z May 1973. The squall line E is now producing funnel clouds and tornadoes along its entire length. Moderate thunderstorms are occurring along the cold front in northwestern Oklahoma and the thunderstorm complex in central Kansas.

Figure C6. ATS III, 26/2201Z May 1973. The fatality-producing tornado occurred near 2200Z at F in the southern end of the squall line. Large tornadoes were also reported near 2200Z at G.